Dynamical evolution of stellar-mass black holes in dense stellar clusters: estimate for merger rate of binary black holes originating from globular clusters

A. Tanikawa[1,2,3]⋆

[1] *RIKEN Advanced Institute for Computational Science 7–1–26, Minatojima-minami-machi, Chuo-ku, Kobe, Hyogo, 650–0047, Japan*
[2] *School of Computer Science and Engineering, University of Aizu, Tsuruga Ikki-machi Aizu-Wakamatsu, Fukushima, 965-8580, Japan*
[3] *Center for Computational Sciences, University of Tsukuba, 1–1–1, Tennodai, Tsukuba, Ibaraki 305–8577, Japan*

ABSTRACT
We have performed N-body simulations of globular clusters (GCs) in order to estimate a detection rate of mergers of Binary stellar-mass Black Holes (BBHs) by means of gravitational wave (GW) observatories. For our estimate, we have only considered mergers of BBHs which escape from GCs (BBH escapers). BBH escapers merge more quickly than BBHs inside GCs because of their small semi-major axes. N-body simulation can not deal with a GC with the number of stars $N \sim 10^6$ due to its high calculation cost. We have simulated dynamical evolution of small-N clusters ($10^4 \lesssim N \lesssim 10^5$), and have extrapolated our simulation results to large-N clusters. From our simulation results, we have found the following dependence of BBH properties on N. BBHs escape from a cluster at each two-body relaxation time at a rate proportional to N. Semi-major axes of BBH escapers are inversely proportional to N, if initial mass densities of clusters are fixed. Eccentricities, primary masses, and mass ratios of BBH escapers are independent of N. Using this dependence of BBH properties, we have artificially generated a population of BBH escapers from a GC with $N \sim 10^6$, and have estimated a detection rate of mergers of BBH escapers by next-generation GW observatories. We have assumed that all the GCs are formed 10 or 12 Gyrs ago with their initial numbers of stars $N_{\rm i} = 5 \times 10^5 - 2 \times 10^6$ and their initial stellar mass densities inside their half-mass radii $\rho_{\rm h,i} = 6 \times 10^3 - 10^6 M_\odot {\rm pc}^{-3}$. Then, the detection rate of BBH escapers is $0.5 - 20$ yr^{-1} for a BH retention fraction $R_{\rm BH} = 0.5$. A few BBH escapers are components of hierarchical triple systems, although we do not consider secular perturbation on such BBH escapers for our estimate. Our simulations have shown that BHs are still inside some of GCs at the present day. These BHs may marginally contribute to BBH detection.

Key words: globular clusters: general – binaries: close – gravitational waves – stellar dynamics – methods: numerical

1 INTRODUCTION

Gravitational wave (GW) observation is greatly expected to open up new fields in physics. Several ground-based GW observatories, such as initial LIGO (Abbott et al. 2009), Virgo (Acernese et al. 2008), GEO600 (Lück et al. 2006), and TAMA300 (Takahashi et al. 2004), have operated, and next-generation observatories, such as advanced LIGO (Harry et al. 2010), advanced Virgo (Accadia et al. 2011), and KAGRA (Kuroda et al. 2010), will start to run in the next several years. For these observatories, mergers of

compact-object binaries are one of the most promising GW sources, where the compact-object binaries consist of stellar-mass black holes (BHs) and neutron stars (NSs). Especially, binaries with two BHs (hereafter, Binary BHs: BBHs) have been not yet found, since they emit little electromagnetic wave. Detection of BBHs will have invaluable impacts on astronomy and astrophysics.

For design of these observatories, it is important to make predictions of a merger rate of BBHs as well as their chirp mass and mass ratio distributions. Once GWs from BBH mergers are detected, these predictions can constrain formation and evolution of BH progenitors, i.e. massive stars. The evolution of the massive stars is, for example, stel-

⋆ E-mail: ataru.tanikawa@riken.jp

lar wind and supernova explosion. Furthermore, these predictions should make clear whether GW detection can identify a dominant BBH formation channel (Sadowski et al. 2008, e.g.) (S08). Theoretically, BBHs are thought to be formed through two channels. One channel is BBH formation from a primordial binary through stellar and binary evolution. In this channel, BBHs are formed dominantly on galactic fields. The other is dynamical formation through a dissipative two-body encounter, three-body encounter among three single stars, binary-single encounter, and so on. The dynamical formation channel happens only in dense stellar clusters, such as globular clusters (GCs), young massive stellar clusters, and nuclear stellar clusters.

So far, many efforts have been devoted to estimate detection rates of BBHs formed in both the channels. Belczynski et al. (2007) have estimated that a detection rate of BBHs formed through the former channel by means of advanced LIGO is 2 yr^{-1}, although they has reported the detection rate of $\sim 10^4$ yr^{-1} (Belczynski & Dominik 2012). On the other hand, Portegies Zwart & McMillan (2000) (PZM00) have predicted that BBHs originating from GCs merge frequently, and that their mergers greatly contribute to GW detection. Following PZM00, various studies estimate detection rates of BBH mergers. Their detection rates are not necessarily consistent with each other: $1 - 10$ yr^{-1} (O'Leary et al. 2006) (O06), $25 - 3000$ yr^{-1} (S08), and $1 - 100$ yr^{-1} (Downing et al. 2010, 2011) (D10 and D11, respectively). Banerjee, Baumgardt & Kroupa (2010) (B10) have reported that the next-generation GW observatories detect mergers of BBHs formed in young massive stellar clusters, rather than in GCs. O'Leary, Kocsis & Loeb (2009) have proposed that mergers of BBHs formed in nuclear stellar clusters are significant. These BBHs are detected by means of advanced LIGO at a rate of $1 - 10$ yr^{-1}. Although the former channel seems to form detectable BBHs more efficiently than the latter channel, an estimate for a BBH detection rate is sensitive to details of underlying models (Dominik et al. 2012). It is worth while to investigate a detection rate of mergers of BBHs formed through the latter channel because of the simpleness of this channel. This channel involves only Newtonian gravity (or low-order post-Newtonian gravity) on the very moment of BBH formation.

In this paper, we especially focus on BBHs formed in GCs. In order to deal with BBH formation, many previous studies approximate GC dynamical evolution in various ways. O06 and S08 follow BH evolution in a GC with a fixed stellar density, determine whether a given BH interacts with other single and binary stars by Monte Carlo technique, and integrate numerically their orbits in the interaction. D10 and D11 follow BH interactions in a Monte Carlo technique similar to the above two studies, however treat numerically GC dynamical evolution by Monte Carlo method (Hénon 1971; Stodółkiewicz 1982, 1984; Giersz 1998). These methods are very convenient to survey vast parameter space of GC initial conditions and stellar evolution because of their low calculation costs, although their calculation costs differ in degree. However, BH dynamics affects stellar densities of GCs, and BBHs may be formed through more complicating interactions than three-body interactions among single stars, binary-single interactions, and binary-binary interactions. For example, six single stars involve binary formation, even if

all stars have equal masses (Tanikawa, Hut & Makino 2012; Tanikawa et al. 2012b).

N-body simulation can solve BH and GC dynamical evolution self-consistently. However, it is practically impossible to treat an *N*-body model with $N \sim 10^6$, comparable to the number of stars in a real GC, due to its large calculation cost. B10 have followed dynamical evolution of stellar clusters with $N \sim 10^5$, and have estimated a BBH merger rate in young massive stellar clusters, not in GCs. PZM00 have performed *N*-body simulations of stellar clusters with several thousand stars, and have extrapolated a BBH merger rate in a GC from their small-*N* results. However, such an extrapolation from small N to large N may involve difficult problems.

In this paper, we focus on, and verify *N*-dependence of BH dynamics in a GC by means of *N*-body simulation. We investigate BBHs which escape from GCs (hereafter, BBH escapers) in detail. BBH escapers merge more quickly than BBHs inside GCs, since the former has smaller semi-major axes than the latter. Using our simulation results, we estimate a BBH detection rate, and predict detected BBH properties , such as distributions of chirp masses and mass ratios of BBH escapers. We also investigate effects of a BH retention fraction.

This paper is organised as follows. In section 2, we describe our *N*-body simulation method. In section 3, we show our simulation results. In section 4, we estimate BBH detection rates by means of GW observatories, based on our simulation results shown in section 3. In section 5, we discuss our estimate. Finally, we summarise this paper in section 6.

2   METHOD

We summarise our simulation models in Table 1. We choose the initial number of cluster stars as $N_i = 8k$, $16k$, $32k$, $64k$, and $128k$, where $1k = 1024$. We adopt Kroupa's function (Kroupa 2001) for a stellar initial mass function, given by

$$f(m)dm \propto \begin{cases} m^{-1.3}dm & (m < 0.5M_\odot) \\ m^{-2.3}dm & (m > 0.5M_\odot) \end{cases} . \tag{1}$$

We set maximum and minimum stellar masses to $50M_\odot$ and $0.1M_\odot$, respectively. We include only single stars, and no primordial binaries for simplicity. In this setup, the average stellar mass of all the clusters is $0.61M_\odot$ at the initial time. These stars are distributed according to King's model (King 1966) with dimensionless concentration parameter $W_0 = 7$. We introduce no primordial mass segregation. Initial virial radii of these clusters, $r_{v,i}$, are shown in the second column of Table 1, and are determined so as to set initial mass densities inside half-mass radii, $\rho_{h,i}$, to 25, 400, and $6400M_\odot \mathrm{pc}^{-3}$, regardless of N_i. The initial mass density, $\rho_{h,i}$, is written in the third column of Table 1. Hereafter, an unit of the stellar mass density is $M_\odot \mathrm{pc}^{-3}$, unless it is explicitly stated otherwise. We adopt stellar metallicity as $Z = 0.001$ which is one of two peaks of the metallicity distribution of the galactic GC system (S08) and GC systems in bright cluster galaxies (Harris et al. 2006).

The clusters are embedded in an external tidal field of their parent galaxy. The parent galaxy has a profile of flat circular velocity. The circular velocity is set to 220 km s^{-1}. Our clusters move around the parent galaxy on a circular

Table 1. Summary of simulation models. Units of $r_{v,i}$ and $\rho_{h,i}$ are pc and $M_\odot \mathrm{pc}^{-3}$, respectively.

N_i	$r_{v,i}$	$\rho_{h,i}$	R_{BH}	N_{run}	$N_{BH,tot,i}$	$N_{BH,i}$	$N_{BBH,tot,esc}$	$N_{BBH,esc}$	$N_{CE-BBH,tot,esc}$
$8k$	3.63	25	1.0	16	197	$7 - 14$	29	$0 - 3$	0
$16k$	4.57	25	1.0	8	188	$19 - 26$	24	$3 - 3$	0
$32k$	5.76	25	1.0	4	181	$42 - 48$	23	$5 - 7$	0
$64k$	7.26	25	1.0	2	187	$92 - 93$	21	$10 - 11$	0
$128k$	9.15	25	1.0	1	178	$-$	23	$-$	0
$8k$	1.44	400	1.0	16	190	$7 - 17$	32	$0 - 4$	1
$16k$	1.81	400	1.0	8	183	$19 - 26$	34	$3 - 6$	1
$32k$	2.28	400	1.0	4	180	$42 - 47$	28	$5 - 8$	0
$64k$	2.89	400	1.0	2	187	$93 - 94$	26	$11 - 15$	0
$8k$	0.57	6400	1.0	16	142	$4 - 15$	25	$0 - 4$	7
$16k$	0.72	6400	1.0	8	145	$17 - 23$	22	$1 - 5$	6
$32k$	0.91	6400	1.0	4	164	$38 - 45$	26	$6 - 8$	4
$64k$	1.14	6400	1.0	2	178	$87 - 91$	28	$13 - 15$	0
$64k$	7.26	25	0.5	4	180	$41 - 55$	25	$5 - 9$	0
$64k$	2.89	400	0.5	4	182	$41 - 56$	28	$6 - 8$	1
$64k$	1.14	6400	0.5	4	179	$41 - 53$	25	$4 - 8$	2
$64k$	7.26	25	0.25	8	189	$14 - 34$	27	$0 - 6$	0
$64k$	2.89	400	0.25	8	193	$16 - 34$	32	$3 - 5$	0
$64k$	1.14	6400	0.25	8	180	$16 - 32$	26	$1 - 5$	2

orbit at the distance of 8.5 kpc from the galactic centre. In this external tidal field, the clusters with $\rho_{h,i} = 25$ have King's cutoff radii equal to Jacobi radii. Here, we define the King's cutoff radius as the distance between the cluster centre and a point at which the stellar density drops off into zero, and the Jacobi radius as the distance between the cluster centre and the Lagrangian point (L1 or L2). This external tidal field is typical for some of the galactic GCs.

As described in detail below, we actually use NBODY4 (Aarseth 2003) for our N-body simulations. A stellar evolution model we adopt is attached to NBODY4, although we change the stellar evolution model in part. We choose stellar and binary evolution models described in Hurley, Pols & Tout (2000) and Hurley et al. (2001), respectively. However, we choose mass losses of massive stars at their supernova explosions from Eldridge & Tout (2004). In the case of $Z = 0.001$, zero-age main-sequence (ZAMS) stars with $6.3 - 21 M_\odot$ leave NSs with $1.44 M_\odot$. ZAMS stars with more than $21 M_\odot$ become BHs, and the relation between ZAMS and BH masses is shown in Fig. 1. Fractions of the numbers of NSs and BHs to the total number of cluster stars are about 1 and 0.2 per cent, respectively.

NSs and BHs should receive natal kicks due to asymmetric supernova explosions. Since velocities of the natal kicks frequently exceeds escape velocities of GCs, a significant fraction of NSs and BHs escape from GCs. We model the natal kick as follows. A part of NSs and BHs receive the natal kicks whose velocities exceed escape velocities of clusters. These NSs and BHs are chosen by means of Monte Carlo technique. NSs and BHs retained in the clusters receive no natal kick at all. Note that the initial velocity distribution of BHs may be different from that in reality due to such treatments for natal kicks. The retention fraction is $R_{NS} = 0.1$ for the case of NSs (Pfahl, Rappaport & Podsiadlowski 2002). Our choice of a BH retention fraction, R_{BH}, is shown in the fourth column of Table 1, which is consistent with $40 - 70$ per cent (Belczynski et al. 2006;
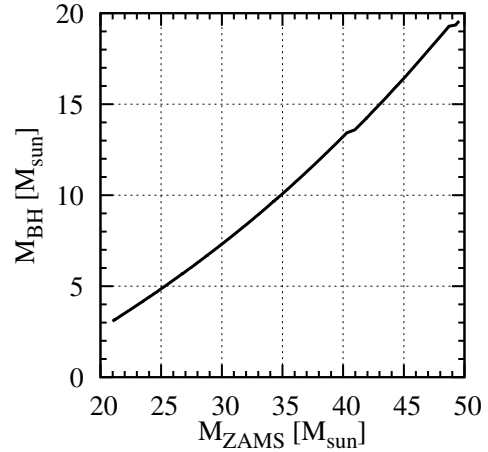
Figure 1. Relation between ZAMS and BH masses. A symbol M_{sun} in this figure is equivalent to $M_\odot$ in the main text, which is the case in the other figures.

Portegies Zwart, McMillan & Makino 2007). The retention fractions of NSs and BHs are assumed to be independent of ZAMS and remnant masses for simplicity. Finally, we draw the BH mass function of our simulation models in Fig. 2. The BH mass function is independent of R_{BH}.

Using different random seeds, we perform several runs for each simulation model. The number of runs (N_{run}) is determined, such that the total number of BHs without natal kick in each simulation model, $N_{BH,tot,i}$, is the same among all the simulation models. Then, N_{run} is inversely proportional to N_i and R_{BH}. The number of runs is shown in the fifth column of Table 1. At each simulation model, $N_{BH,tot,i}$ is about $140 - 200$, described in the sixth column of Table 1. We also give the maximum and minimum numbers of BHs without natal kick among runs at each simulation model, $N_{BH,i}$, in the seventh column of Table 1.
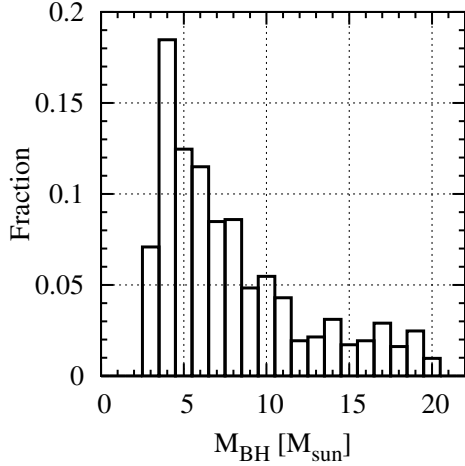
Figure 2. BH mass function of our simulation models.

We use the `NBODY4` code for our N-body simulations. The `NBODY4` code adopts fourth-order Hermite scheme with individual timestep, and treat close encounters between two stars by KS regularization (Kustaanheimo & Stiefel 1965), and those among more than two stars by chain regularization (Mikkola & Aarseth 1990, 1993).

We accelerate calculation of gravitational forces in the `NBODY4` code by using Graphic Processing Units (GPUs) with the `Yebisu` code (Nitadori 2009). Since the `Yebisu` code does not originally deal with no softened gravitational potential, we modify the code so that it supports no softening force shape. We also accelerate a search for neighbour particles around a given particle by using SIMD instructions, here Advanced Vector eXtensions (AVX), with Phantom-GRAPE for a collisional version (Tanikawa et al. 2012a). We parallelise the calculation of gravitational forces with Message Passing Interface (MPI), such that we divide particles exerting gravitational forces on a given particle into MPI processes, which is so-called j-parallel algorithm. We search for neighbour particles in parallel in the same way as the calculation of gravitational forces.

All of our runs are performed on "HA-PACS", which is a supercomputer system at Center for Computational Sciences in University of Tsukuba. One node of HA-PACS is configured as two Intel E5 CPUs and four Nvidia M2090 GPUs. The nodes are connected in a fat-tree network with Infiniband QDRx2. We use one node for simulation models with $N_i = 8k$, $16k$, and $32k$, two nodes for simulation models with $N_i = 64k$, and four nodes for simulation models with $N_i = 128k$. Simulation models with $N_i = 64k$ and $\rho_{h,i} = 6400$ are the most time-consuming. The wall-clock time for each simulation is about 300 hours.

Finally, we mention several units used in the following sections. First, we often use a thermodynamical time, τ, given by

$$\tau = \int_0^t \frac{dt'}{t_{rh}}, \qquad (2)$$

where t is a physical time, and t_{rh} is an instantaneous half-mass relaxation time at t. The half-mass relaxation time is

defined as

$$t_{rh} = 0.0477 \frac{N}{(G\rho_h)^{1/2} \log(0.4N)}, \qquad (3)$$

where G is the gravitational constant, N is the number of stars of a cluster at t, and ρ_h is a mass density inside a half-mass radius of the cluster at t (Spitzer 1987). The thermodynamical time τ can be called as "the elapsed number of actual half-mass relaxation time", which is similar to "the elapsed number of actual central relaxation time described at eq. (4) of Cohn, Hut & Wise (1989) (Takahashi 1996, see also). Next, we describe units related to binaries. We introduce an energy unit, kT_i, where $3/2kT_i$ is the average kinetic energy of cluster stars at the initial time. Then, we can write $1kT_i$ as

$$1kT_i = \frac{1}{6N_i} \frac{GM_i^2}{r_{v,i}}. \qquad (4)$$

Furthermore, we introduce a_{1kT_i} as a length unit. A binary has its semi-major axis a_{1kT_i}, when it has its binding energy $1kT_i$ and component masses, both of which are the average stellar mass at the initial time. The semi-major axis a_{1kT_i} is given by

$$a_{1kT_i} = \frac{3}{N_i} r_{v,i}. \qquad (5)$$

3 SIMULATION RESULTS

3.1 Thermodynamical evolution

In this section, we investigate a relation between a physical time t and a thermodynamical time τ given by equation (2). A pure N-body system is scale-free, and is evolved only by two-body relaxation, which results from gravitational interactions between stars. Our simulation models include stellar evolution, and are not pure N-body systems. Nevertheless, our simulation models have aspects of pure N-body systems. In fact, BHs and BBHs in clusters with different N_i and $\rho_{h,i}$ evolve similarly in terms of τ, as shown in section 3.2. The thermodynamical time τ is an indicator for dynamical states of clusters with different N_i and $\rho_{h,i}$. Converting τ to t, we can know states of BHs and BBHs of a cluster at a given physical time, even if the cluster have N_i and $\rho_{h,i}$ which we do not adopt in our simulations.

Fig. 3 shows relations between t and τ in all the runs. These relations are almost the same among all the runs in each simulation model. Clusters with different random seeds evolve similarly to each other in terms of thermodynamics. Relations between t and τ are also similar among simulation models with different R_{BH} (see the bottom panels of Fig. 3). Even if R_{BH} is different, cluster evolution is thermodynamically similar. In other words, N and ρ_h evolve similarly. This is because the total number and mass of BHs are much smaller than those of cluster stars.

3.2 BH and BBH evolution

In this section, we show BH and BBH evolution in terms of τ. Fig. 4 shows the time evolution of the numbers of BHs in clusters, $N_{BH,tot}$. The number $N_{BH,tot}$ is the summation of the numbers of BHs of all the runs in each simulation model, not the number of BHs in each run. First, we focus
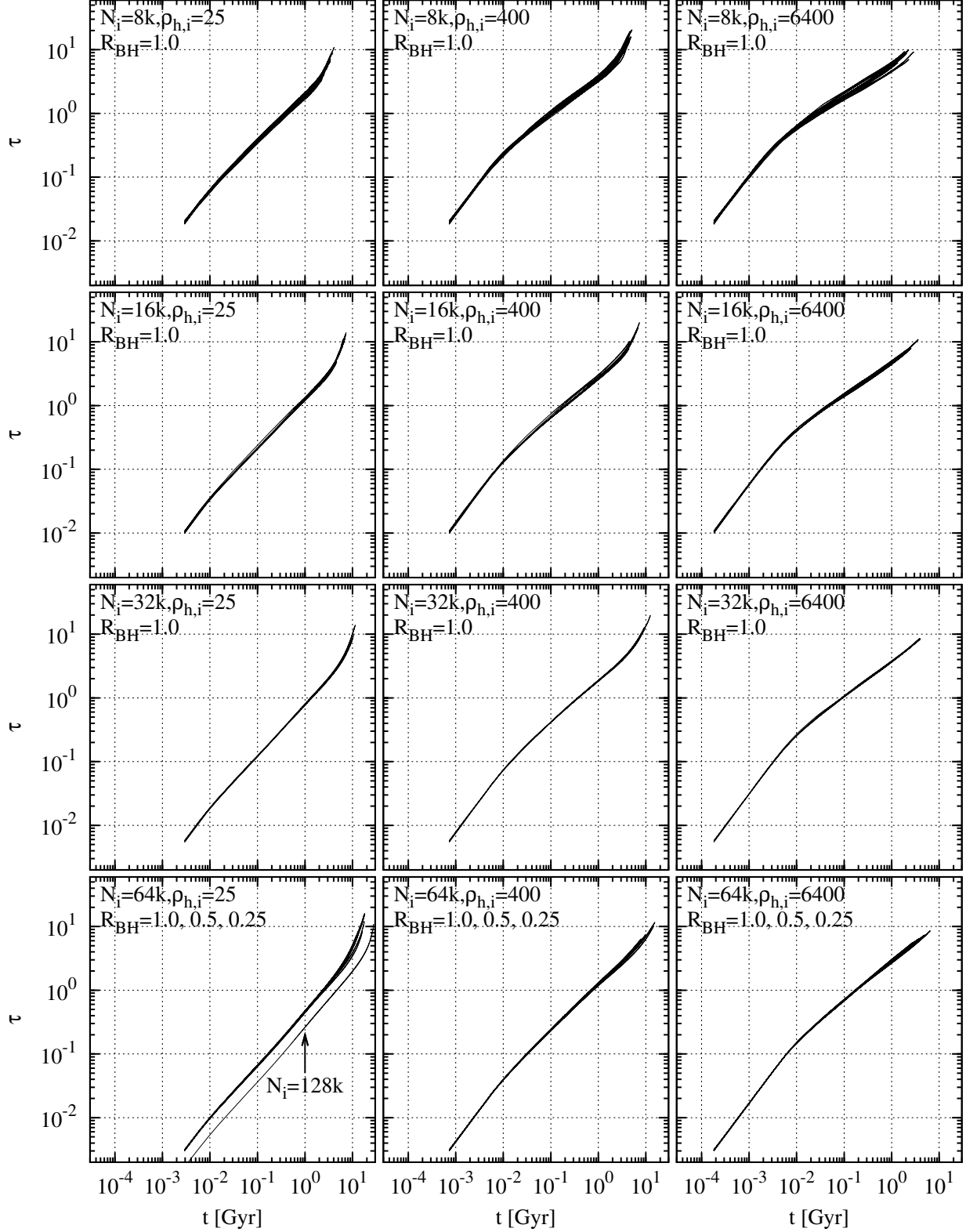
Figure 3. Relation between a physical time, t, and a thermodynamical time, τ, in all the runs. Simulation models are indicated in each panel, except a simulation model with $N_{\rm i} = 128k$, $\rho_{\rm h,i} = 25$ and $R_{\rm BH} = 1.0$, which is pointed to by the arrow. The panels of $N_{\rm i} = 64k$ include all the simulation models with $R_{\rm BH} = 1.0$, 0.5, and 0.25, and the other panels include only simulation models with $R_{\rm BH} = 1.0$.

on simulation models with the same $\rho_{\mathrm{h,i}}$ and R_{BH}, and different N_{i} (see each of the top panel in Fig. 4). We can see that $N_{\mathrm{BH,tot}}$ decreases in a similar manner. This means that the number of BHs which escape from each cluster at each thermodynamical time is proportional to N_{i}. Next, we investigate simulation models with the same $\rho_{\mathrm{h,i}}$ and N_{i}, and different R_{BH} (see each of the bottom panel in Fig. 4). The number $N_{\mathrm{BH,tot}}$ also decreases in a similar manner among different R_{BH} models. The number of BHs which escape from a cluster at each thermodynamical time is proportional to R_{BH}.

We pay attention to dependence of BH evolution on $\rho_{\mathrm{h,i}}$ (see all the top panels of Fig. 4). We draw the same red lines in all the panels of Fig. 4, which fit to models with $\rho_{\mathrm{h,i}} = 6400$ and $R_{\mathrm{BH}} = 1.0$. The red line is expressed as $N_{\mathrm{BH,tot}} = N_{\mathrm{BH,tot,i}}(1 - 0.15\tau)$, where $N_{\mathrm{BH,tot,i}} = 190$, which is consistent with our simulation models (see the sixth column of Table 1). Note that this is just a simple fitting. We do not claim that there is some physics behind it. The red line is in good agreement with BH evolution of models with $\rho_{\mathrm{h,i}} = 400$ and $R_{\mathrm{BH}} = 1.0$ before $\tau = 6$. At first glance, the red line does not seem to be at all in agreement with BH evolution of models with $\rho_{\mathrm{h,i}} = 25$ and $R_{\mathrm{BH}} = 1.0$ all the time. However, decrease rates of $N_{\mathrm{BH,tot}}$ at $\tau = 0$ and 6 in these models are, respectively, larger and smaller than that of the red line only by a factor of about 2. The decrease rates of $N_{\mathrm{BH,tot}}$ are different at most by a factor of 2, despite that $\rho_{\mathrm{h,i}}$ ranges from 25 to 6400. We can regard that BHs evolve almost independently of $\rho_{\mathrm{h,i}}$. In summary, BHs escape from a cluster at a rate proportional to N_{i} and R_{BH}, and at a rate independent of $\rho_{\mathrm{h,i}}$ in the unit of τ. Therefore, we can give the time evolution of the number of BHs in a cluster as follows:

$$N_{\mathrm{BH}}(\tau) = N_{\mathrm{BH,i}} \left(1 - 0.15\tau\right). \tag{6}$$

The eighth and ninth columns of Table 1 show the total number of BBH escapers in each simulation model, and the minimum and maximum numbers of BBH escapers among all the runs of each simulation model, respectively. The total number of BBH escapers, $N_{\mathrm{BBH,tot,esc}}$, is not dominated by only one of runs in any simulation models. The difference of the number of BBH escapers among runs in each simulation model is small. This difference comes from the difference of the number of BHs without the natal kick, and from statistical fluctuation, not from the difference of global evolution among runs.

Fig. 5 shows the time evolution of the cumulative number of BBH escapers, $N_{\mathrm{BBH,esc,tot}}$. The number $N_{\mathrm{BBH,esc,tot}}$ is the summation of the numbers of BBH escapers of all the runs in each simulation model, not the number of BBH escapers in each run. As seen in each panel of Fig. 5, $N_{\mathrm{BBH,esc,tot}}$ increases in a similar way among models with the same $\rho_{\mathrm{h,i}}$ and R_{BH}, and different N_{i}, and among models with the same $\rho_{\mathrm{h,i}}$ and N_{i}, and different R_{BH}. We fit a red line to $N_{\mathrm{BBH,esc,tot}}$ of models with $\rho_{\mathrm{h,i}} = 6400$ and $R_{\mathrm{BH}} = 1.0$. The red line is expressed as $N_{\mathrm{BBH,esc,tot}} = 0.020N_{\mathrm{BH,tot,i}}\tau$. Note that this is just a simple fitting. We do not claim that there is some physics behind it. During $\tau = 0 - 5$, the red lines are in good agreement with $N_{\mathrm{BBH,esc,tot}}$ in all the models. In summary, BBHs escape from a cluster in a rate proportional to N_{i} and R_{BH}, and at a rate independently of $\rho_{\mathrm{h,i}}$, which is similar to BH evolution. At least during $\tau = 0 - 5$, we can give the time evolution of the cumulative number of BBH escapers as follows:

$$N_{\mathrm{BBH,esc}}(\tau) = 0.020N_{\mathrm{BH,i}}\tau. \tag{7}$$

We use equations (7) only for an estimate of a BBH detection rate in section 4. The fitting is in good agreement with our simulation results during $\tau = 0 - 5$ in all the models, and during $\tau = 0 - 8$ in models with $\rho_{\mathrm{h,i}} = 400$ and 6400. We do not mind that the red lines are slightly deviated from our simulation results in models with $\rho_{\mathrm{h,i}} = 25$ after $\tau = 5$. These clusters are evaporated strongly in contrast to those in models with $\rho_{\mathrm{h,i}} = 400$ and 6400. In section 4, we estimate the detection rate of BBH escapers from clusters with $\rho_{\mathrm{h,i}}$ larger than 6400, which are evaporated less than clusters with $\rho_{\mathrm{h,i}} = 6400$. The number of BBH escapers from these clusters should evolve similarly to clusters in models with $\rho_{\mathrm{h,i}} = 400$ and 6400.

We can explain why the numbers of BH and BBH escapers at each thermodynamical time are proportional to N_{i} as follow. After BHs and NSs are formed, stars do not evolve so active. Our simulation models can be regarded as nearly pure N-body systems. Therefore, our simulation models are scale-free, and evolved by two-body relaxation. At each thermodynamical time, a constant fraction of the total energy of a cluster flows out from the cluster through two-body relaxation. If there is no energy source at the cluster core, the core continues to shrink, and its density grows. At some point, binaries are formed because of high density at the core. The binaries interact with other single and binary stars in a superelastic manner. Such interactions result in ejections of other stars and binaries themselves. These ejections indirectly heat the cluster, since the cluster loses binding energies of ejected stars. This indirect heating is balanced with the energy outflowing through two-body relaxation, so that the core stops shrinking. Therefore, the cluster loses a constant fraction of its total mass through the ejections of single and binary stars at each thermodynamical time. Since the mass lost by the cluster contains a constant fraction of BHs, the number of BH escapers is proportional to N_{i} at each thermodynamical time, which can be true of BBH escapers.

The numbers of BH and BBH escapers at each thermodynamical time are proportional to R_{BH}. This is because the mass lost by a cluster contains a fraction of BHs, proportional to R_{BH}. Since clusters with different R_{BH} evolve similarly in terms of τ (see the bottom panels of Fig. 3), BBHs should be formed similarly among these clusters. However, BBH escape rates are proportional to R_{BH}. Therefore, a given BBH stays for a longer time in a cluster with smaller R_{BH}. This may be because there are fewer BHs to scatter with in these clusters (Mackey et al. 2008). This dependence on R_{BH} seems consistent with simulation results of Breen & Heggie (2013), when we compare points with the same sizes and symbols between filled and unfilled ones in fig. 8. As a BBH stays for a longer time in a cluster, the BBH emits larger energy, and its binding energy becomes larger. Consequently, BBH escapers from clusters with smaller R_{BH} should have larger binding energies. Actually, this is consistent with our simulation results. Fig. 6 shows the cumulative distribution of binding energies of BBH escapers. In each panel, we can see that BBH escapers in models with smaller R_{BH} have larger binding energies.
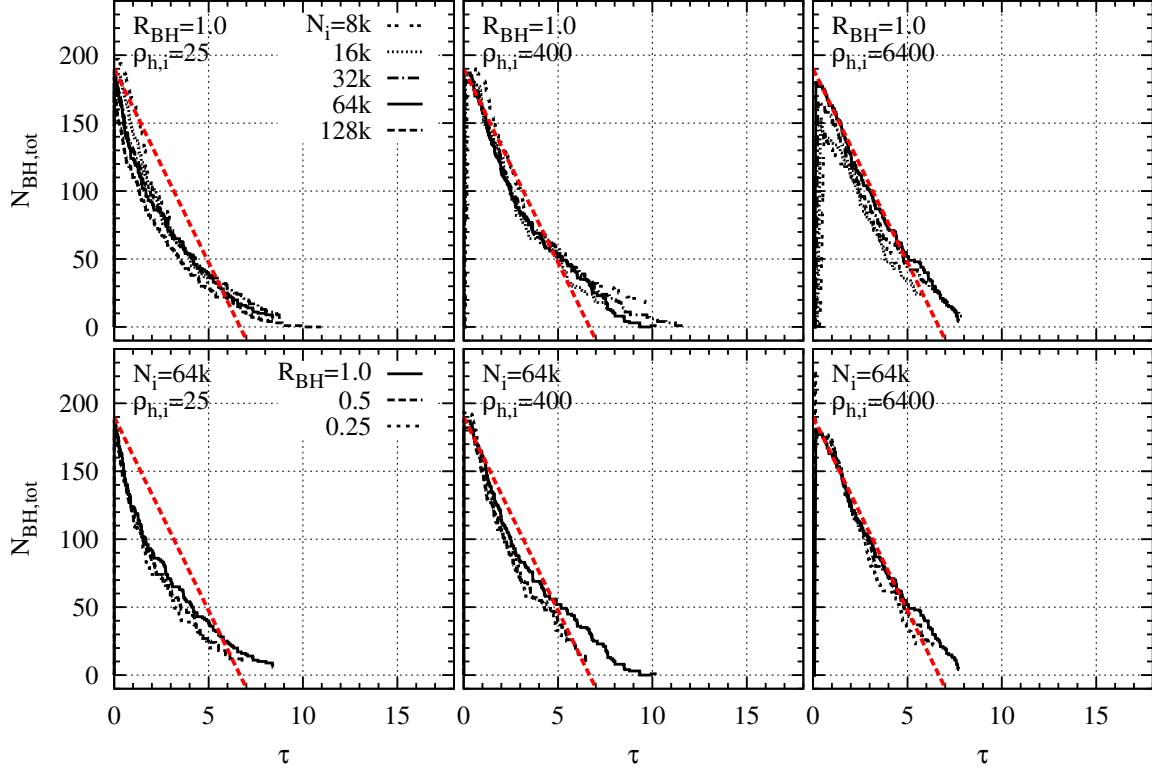
Figure 4. Time evolution of the numbers of BHs in the clusters. The number is the summation of the numbers of BHs of all the runs in each simulation model, not the number of BHs in each run. The horizontal axis is a thermodynamical time, τ, defined as equation (2). Curve with the same line types indicate the same N_i among the top panels, and the same R_{BH} among the bottom panels. Red dashed line in each panel shows $N_{BH,tot} = N_{BH,tot,i}(1 - 0.15\tau)$, where $N_{BH,tot,i} = 190$.

3.3 Properties of BBH escapers

In this section, we investigate orbital elements and mass components of BBHs, which determine a merging timescale through GW. We focus on BBH escapers. The most hardest binaries in a cluster are the most likely to be ejected due to recoil during an interaction. These binaries have the smallest semi-major axes, if all the binaries have BHs with the same masses. BBH escapers merge more quickly than BBHs inside GCs.

We show the cumulative distribution of semi-major axes of BBH escapers in Fig. 7. First, we take a look at their dependence on N_i among each simulation model with the same $\rho_{h,i}$ and R_{BH} (see each of the top panels of Fig. 7). In simulation models with $\rho_{h,i} = 25$ and 400, their cumulative distributions are independent of N_i in the unit of a_{1kT_i}. In simulation models with $\rho_{h,i} = 6400$, their cumulative distributions are quite different. 20 percentiles in these models become larger with N_i increasing: $4 \times 10^{-3} a_{1kT_i}$ for $N_i = 8k$ and $16k$, $4 \times 10^{-2} a_{1kT_i}$ for $N_i = 32k$, and $9 \times 10^{-2} a_{1kT_i}$ for $N_i = 64k$. This is because smaller N_i models contain more escapers of BBHs whose formation is involved by common envelope evolution. We call these BBH escapers "CE-BBH escapers". In contrast to CE-BBH escapers, we call escapers of BBHs formed only through an N-body process "NB-BBH escapers".

These CE-BBHs are formed as follows. Two BH progenitors (or a pair of a BH and BH progenitor) form a binary through three-body interactions. Either of the two evolves off the main sequence, and common envelop evolution occurs. In some of these binaries, common envelope evolution occurs again, when the other star evolves off the main sequence. CE-BBH escapers tend to have smaller semi-major axes than NB-BBH escapers. Common envelope evolution shrink a semi-major axis of a binary, involving no kick on the binary, except BH natal kick. Note that CE-BBHs receive no BH natal kick at a constant rate in our natal kick model. On the other hand, an N-body process, such as a three-body interaction, also shrinks a semi-major axis of a binary, but gives dynamical recoil on the binary. Therefore, NB-BBHs are ejected from the cluster before their semi-major axes become as small as those of CE-BBHs. The top left panel of Fig. 8 shows the cumulative distribution of semi-major axes of only NB-BBH escapers. We can see that their semi-major axes are distributed independently of N_i.

The tenth column of Table 1 indicates the total number of CE-BBH escapers in all the runs of each simulation model. The number of CE-BBHs decreases as N_i increases, and $\rho_{h,i}$ decreases. A CE-BBH escaper has already been a binary before at least one of its components becomes a BH. In order for CE-BBH escapers to be formed, a cluster experiences core collapse before massive stars evolve to BHs. Therefore, the number of CE-BBH escapers decreases in a cluster with longer half-mass relaxation time, i.e. that with larger N_i and smaller $\rho_{h,i}$.
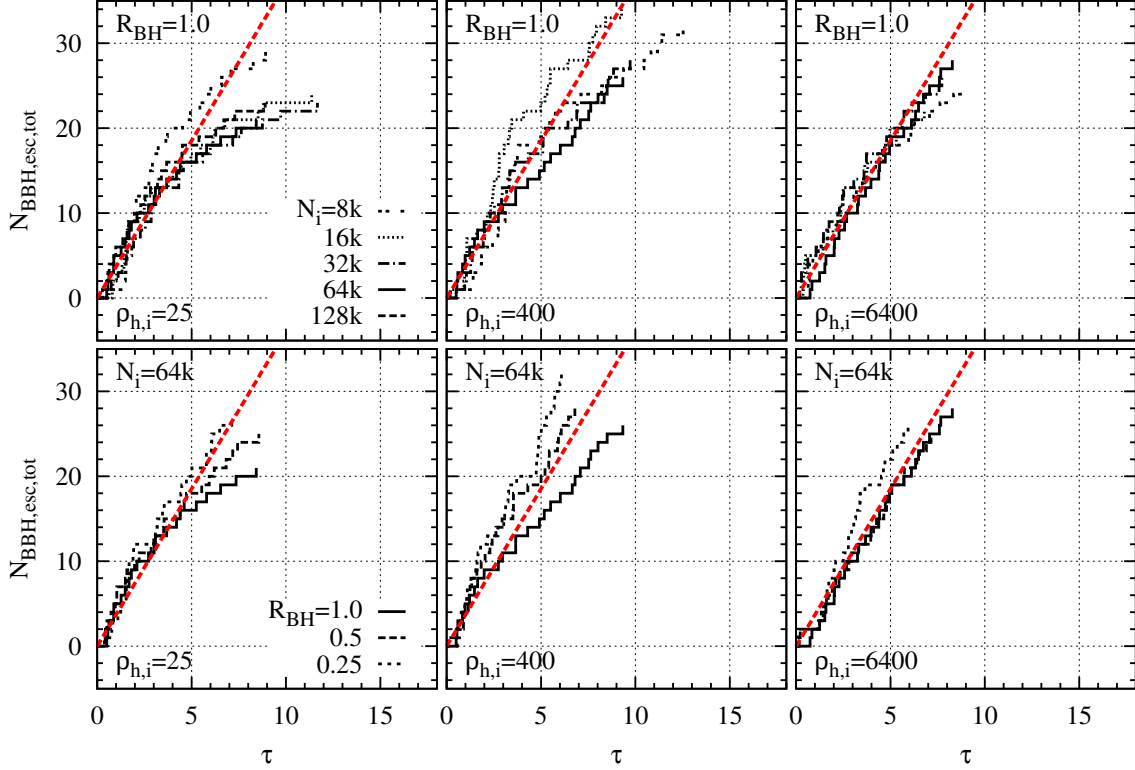
We focus on dependence of semi-major axes of BBH

Figure 5. Time evolution of the cumulative number of BBH escapers. The cumulative number is the summation of the cumulative numbers of BBH escapers of all the runs in each simulation model, not the cumulative number of BBH escapers in each run. The horizontal axes are the same as Fig. 4. Curves with the same line types indicate the same N_i among the top panels, and the same R_{BH} among the bottom panels. Red dashed line in each panel shows $N_{BBH,esc,tot} = 0.020 N_{BH,tot,i} \tau$, where $N_{BH,tot,i} = 190$.
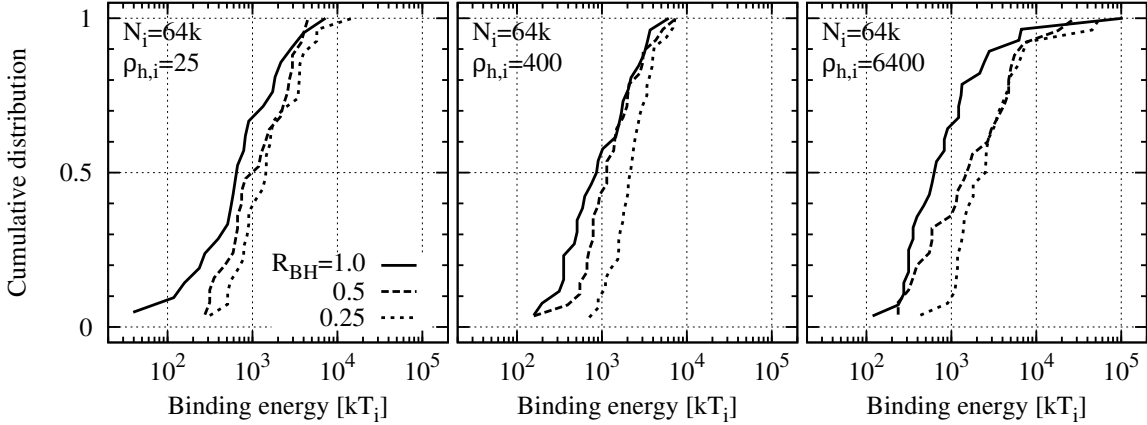
Figure 6. Cumulative distribution of binding energies of BBH escapers in all the runs of each simulation model. The total BBH escapers in all the runs of each simulation model are accumulated, which is the case for all the cumulative distributions in this paper. The unit of binding energies is kT_i, defined as equation (4).

escapers on $\rho_{h,i}$ (see the top left and middle panels of Fig. 7, and the top left panel of Fig. 8). We draw red curves in all these panels. Formula of these red curves is given by

$$P_1(a) = \int_0^a p_1(a') da', \tag{8}$$

where

$$p_1(a) = \frac{1}{\sqrt{2\pi}\sigma(a/a_{1kT_i})}$$

$$\times \exp\left\{-\frac{1}{2\sigma^2}\left[\log\left(\frac{a}{a_{1kT_i}}R_{BH}^{-1/2}\right) - \log\mu\right]^2\right\}. \tag{9}$$

The function $p_1(a)$ is a log-normal distribution with $\sigma =$

0.81 and $\mu = 0.15$. The red curves fit to cumulative distributions of BBH escapers in simulation models with $\rho_{h,i} = 400$ and $R_{BH} = 1.0$ (the top middle panel of Fig. 7), and of NB-BBH escapers in simulation models with $\rho_{h,i} = 6400$ and $R_{BH} = 1.0$ (the top left panel of Fig. 8).

As seen in the bottom panels of Fig. 7, BBH escapers in smaller R_{BH} models have smaller semi-major axes than those in larger R_{BH} models. This is reflected by the fact that BBH escapers in smaller R_{BH} models have larger binding energies than those in larger R_{BH} models (see Fig. 6). The red curves are in good agreement with the cumulative distribution, when the semi-major axes of BBH escapers are are proportional to $R_{BH}^{-1/2}$, as indicated in equation (9). We note that equation (9) is just a simple fitting. We do not claim that there is any physical background for this probability distribution.

Note that the distribution of the semi-major axes in simulation models with $\rho_{h,i} = 25$ is larger than the fitting formula. Clusters with $\rho_{h,i} = 25$ strongly experience mass loss due to evaporation, since external tidal fields are strong for these models. Small escape velocities of these clusters results in ejections of BBHs which are not so hard, i.e. have large semi-major axes. On the other hand, clusters with $\rho_{h,i} = 400$ and 6400 are not evaporated so much. Owing to the fact that pure N-body system is scale-free, the distributions of the semi-major axes of BBH escapers are similar between clusters with $\rho_{h,i} = 400$ and 6400, and are fitted to equation (8). Eventually, we estimate a detection rate of BBH escapers from clusters with $\rho_{h,i}$ larger than 6400 in section 4. These clusters are less evaporated than the clusters with $\rho_{h,i} = 400$ and 6400, since they are more compact. BBH escapers from these clusters should have similar distributions of semi-major axes to this fitting formula. This is the reason why we ignore data of simulation models with $\rho_{h,i} = 25$ for the fitting formula.

So far, we describe semi-major axes of BBH escapers in the units of a_{1kT_i}. Converting the units of a_{1kT_i} to physical units, we can say that semi-major axes of BBH escapers are inversely proportional to N_i, and proportional to the initial size of clusters, such as virial radii (see equation (5)).

We move on to the subject of eccentricities of BBH escapers. We see cumulative distributions of eccentricities of BBH escapers in Fig. 9. The eccentricity distributions in all the simulation models are consistent with the thermal distribution (Heggie 1975), expressed as

$$p_2(e) = 2e. \tag{10}$$

Formula of the red curves in Fig. 9 is expressed as

$$P_2(e) = \int_0^e p_2(e')de'. \tag{11}$$

Although the cumulative distributions are deviated from the function $P_2(e)$, they are centred around it.

Next, we investigate cumulative distributions of primary masses of BBH escapers, which is shown in Fig. 10. The cumulative distributions are independent of N_i, $\rho_{h,i}$, and R_{BH}. We compare the distribution of primary masses of artificially generated BBHs, where we define their distribution as $p_3(m_1)$, and their cumulative distribution as $P_3(m_1)$, where m_1 is the primary BH mass of a BBH escaper. We generate these BBHs as follows. We realise two BBHs whose mass distribution is subject to that shown in

Fig. 2, and choose the more massive BH as the primary BH. The function $P_3(m_1)$, drawn by red curves in Fig. 10, is in good agreement with the cumulative distribution of primary masses of BBH escapers.

We show cumulative distributions of mass ratios, $q = m_2/m_1$, of BBH escapers in Fig. 11, where m_2 is the secondary BH mass of a BBH escaper. Blue dotted curves show the cumulative distribution of the mass ratios of the artificially generated BBHs. Clearly, the blue dotted curves are not at all in agreement with the cumulative distribution in any simulation model. The distributions of the mass ratios rather fit to the following function:

$$P_4(q) = \int_0^q p_4(q')dq', \tag{12}$$

where

$$p_4(q) = 2 \ (0.5 < q < 1), \tag{13}$$

which are indicated by red dashed curves in each panel of Fig. 11. The mass ratio distributions of BBH escapers in our simulations is larger than those of the artificially generated BBHs. This is because more massive BHs are more likely to be at the cluster centre, and to be retained in BBHs after binary-single and binary-binary interactions. In fact, BBHs contain those with $q < 0.5$. However, such BBHs are at most 20 per cent of all the BBHs (simulation models with $\rho_{h,i} = 6400$). This fitting function is sufficiently accurate for rough estimates of BBH mergers described in section 4. We note that equation (13) is just a simple fitting. We do not claim that there is any physical background for this probability distribution.

We mention some properties of NB-BBH escapers in simulation models with $\rho_{h,i} = 6400$ and $R_{BH} = 1.0$. Fig. 8 summarises their properties. Their cumulative distributions of eccentricities, primary masses, and mass ratios fit to each fitting function (see the top right, the bottom left, and the bottom middle panels, respectively). The time evolution of the cumulative number of NB-BBH escapers is also in good agreement with its fitting function for model with $N_i = 64k$ (see the bottom right). This is natural, since the clusters of this model do not include CE-BBH escapers.

Finally, we search for correlations between BBH properties and BBH escape time. Fig. 12 shows primary masses of BBHs which escape from clusters at τ. Apart from CE-BBHs, the primary masses become lighter with time in all the models in a similar way. Before $\tau = 1$, primary masses are about $20M_\odot$, which is maximum mass of BHs without progenitor's mergers. The mass decreases monotonically, and finally becomes about 3 or $4M_\odot$ at $\tau = 10$. CE-BBHs escape at an early time, before $\tau = 1$. They are formed at an early time, and have large binding energies at birth. Therefore, they are ejected from clusters once they interact with other stars. Some of BHs have more than $20M_\odot$, and are formed through mergers of their progenitors. No pair of BHs merges in our simulations. As a simple fitting, we write the evolution of the primary masses of BBH escapers as

$$m_1(\tau) = \begin{cases} 20M_\odot & (0.5 < \tau < 1.5) \\ \\ 20M_\odot \left(\dfrac{\tau}{1.5}\right)^{-1} & (\tau > 1.5) \end{cases}, \tag{14}$$
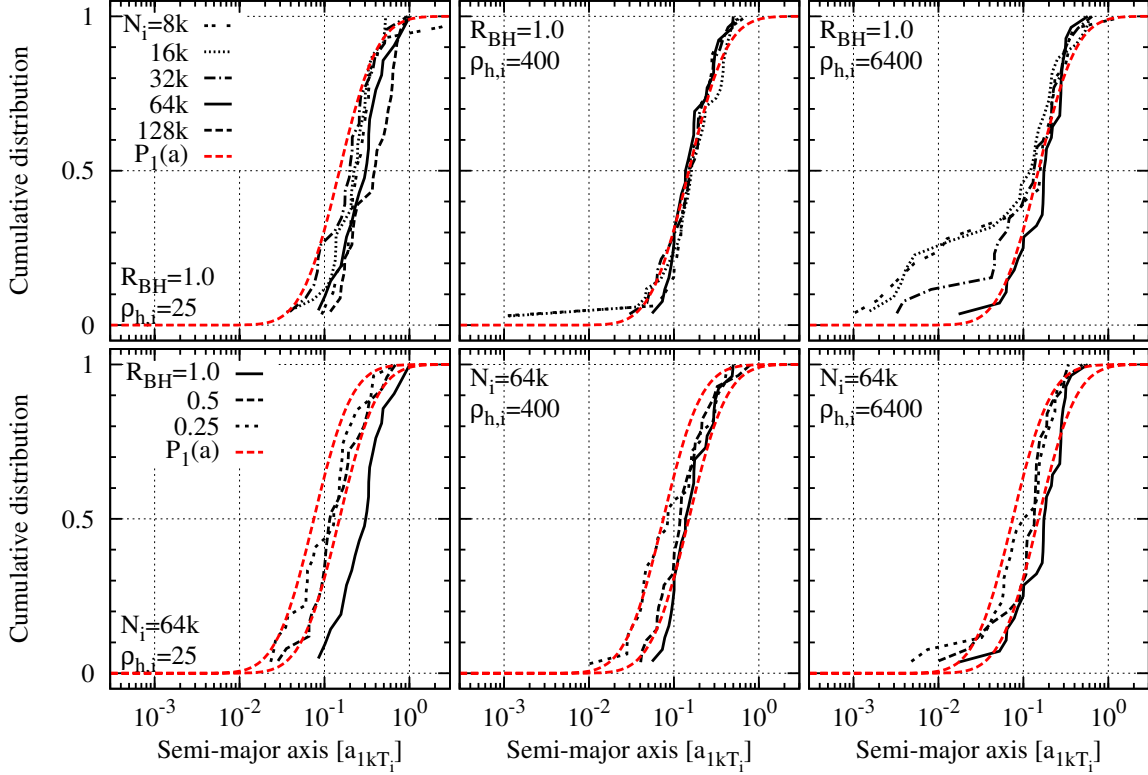
which is indicated by black curves in Fig. 12.

Figure 7. Cumulative distribution of semi-major axes of BBH escapers. The unit of semi-major axes is $a_{1\mathrm{kT_i}}$, defined as equation (5). Curves with the same line types indicate the same N_{i} among the top panels, and the same R_{BH} among the bottom panels. The formula of red curves is expressed as equation (9). $R_{\mathrm{BH}} = 1.0$ is adopted for the red curves in the top panels, and $R_{\mathrm{BH}} = 0.25$ (left red curves) and 1.0 (right red curves) in the bottom panels.

Except the correlation between escape time and primary BH masses, we have found no correlation between any pair of escape time, semi-major axes, eccentricities, primary BH masses, and mass ratios.

4   ESTIMATE FOR BBH DETECTION RATE

In this section, we estimate a detection rate of GWs from mergers of BBHs originating from GCs. In section 4.1, we give a formula for a BBH detection rate, which is similar to those of O06 and D10. Before we solve the formula, we need to adopt parameters related to GCs, which is described in section 4.2. We describe our solution method for the formula in section 4.3. Finally, we show the detection rate and properties of BBH escapers in section 4.4.

4.1   Formula for BBH detection rate

In this section, we estimate a detection rate of BBHs originating from GCs. We consider only NB-BBH escapers as GW sources. BBH escapers merge more easily than BBHs inside GCs. Furthermore, NB-BBH escapers dominate BBH escapers. This reason is described in section 4.2.

We follow the approach of O06 and D10 for obtaining the detection rate. The detection rate is calculated as

$$\Gamma_{\mathrm{det,tot}} = f_{\mathrm{det}}^{-3} \int_{t_{\mathrm{u}}=0}^{t_{\mathrm{u}}=t_{\mathrm{u},0}} \left[n_{\mathrm{gc}} dV(t_{\mathrm{u}}) \frac{\Gamma_{\mathrm{det}}(t_{\mathrm{u}})}{1+z(t_{\mathrm{u}})} \right], \quad (15)$$

which corresponds to equation (13) of O06, and to equation (11) of D10, although their equations have been already discretised. A variable t_{u} is the universe age, and $t_{\mathrm{u},0}$ is the universe age at the present time. A variable $z(t_{\mathrm{u}})$ is a redshift at a universe age t_{u}. A variable $V(t_{\mathrm{u}})$ is the volume of the universe at a universe age t_{u}, which is observed from us. A variable $\Gamma_{\mathrm{det}}(t_{\mathrm{u}})$ is a detection rate of BBH escapers merging at the universe age t_{u}, where the BBH escapers originate from *one* GC. A constant n_{gc} is the number density of GCs in the universe. We adopt $n_{\mathrm{gc}} = 8.4h^3\mathrm{Mpc}^{-3}$ (Portegies Zwart & McMillan 2000), where h is described later. A factor $f_{\mathrm{det}} = 2.26$ considers the non-uniform pattern of detector sensitivity and random sky orientation of sources (Finn & Chernoff 1993). The factor $1/[1+z(t_{\mathrm{u}})]$ comes from a cosmological time dilation of the detection rate. Here, we assume that all GCs are identically formed at the same time, and that the number density of GCs keeps constant at a given universe age t_{u}.

We relate a universe age t_{u} to its redshift $z(t_{\mathrm{u}})$ as

$$t_{\mathrm{u}} = H_0^{-1} \int_z^\infty \frac{dz'}{(1+z')\sqrt{\Omega_{\mathrm{m}}(1+z')^3 + \Omega_\Lambda}} \quad (16)$$

$$= \frac{1}{3H_0\sqrt{\Omega_\Lambda}} \log \left[\frac{\sqrt{\Omega_{\mathrm{m}}(1+z)^3 + \Omega_\Lambda} + \sqrt{\Omega_\Lambda}}{\sqrt{\Omega_{\mathrm{m}}(1+z)^3 + \Omega_\Lambda} - \sqrt{\Omega_\Lambda}} \right], \quad (17)$$

where $H_0 = 100h$ kms^{-1}Mpc^{-1}. We adopt $\Omega_{\mathrm{m}} = 0.28$, $\Omega_\Lambda = 0.72$, and $h = 0.73$, based on WMAP9 (Hinshaw et al. 2012).
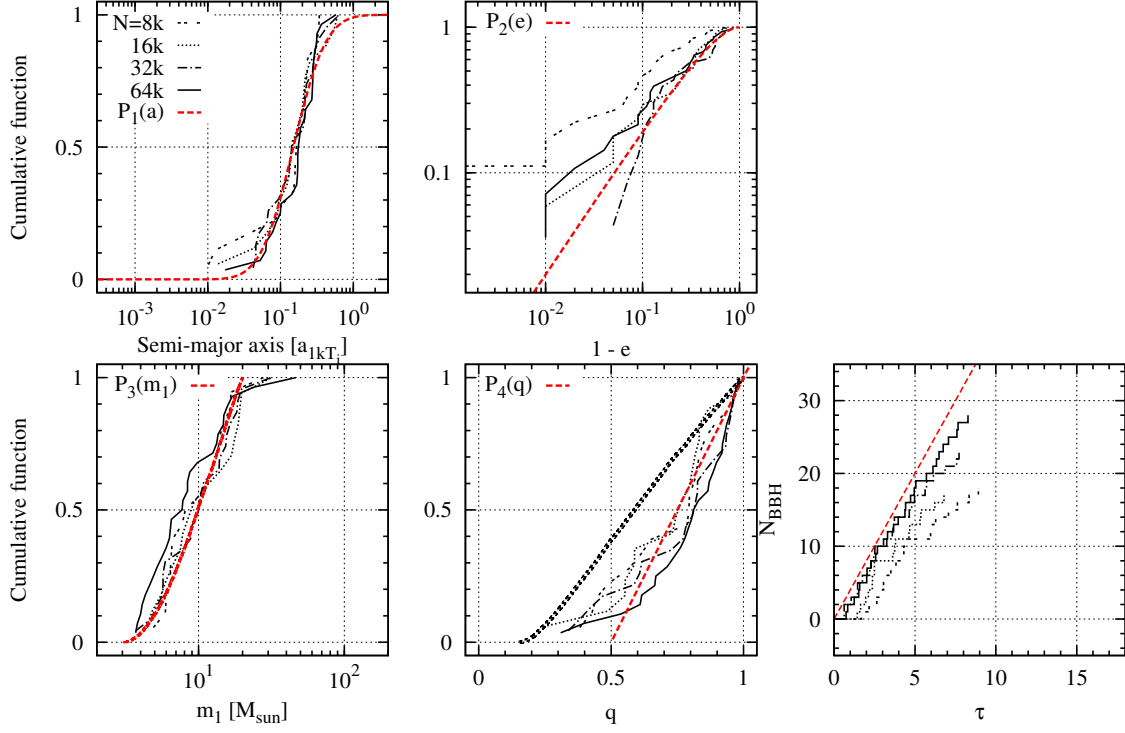
Figure 8. Cumulative distribution of semi-major axes, eccentricities, primary masses, and mass ratios of NB-BBHs, and time evolution of the cumulative number of NB-BBHs in models with $\rho_{h,i} = 6400$ and $R_{BH} = 1.0$. The red dashed line in the bottom right panel is identical with those in Figure 5.

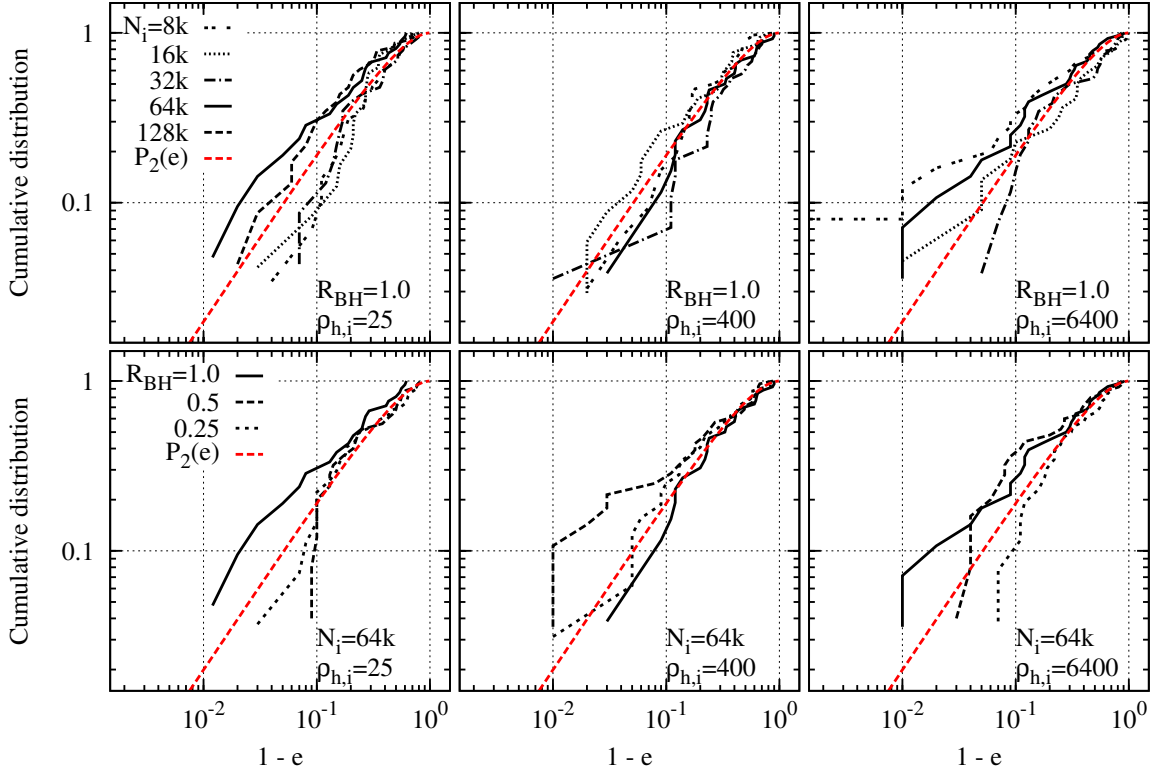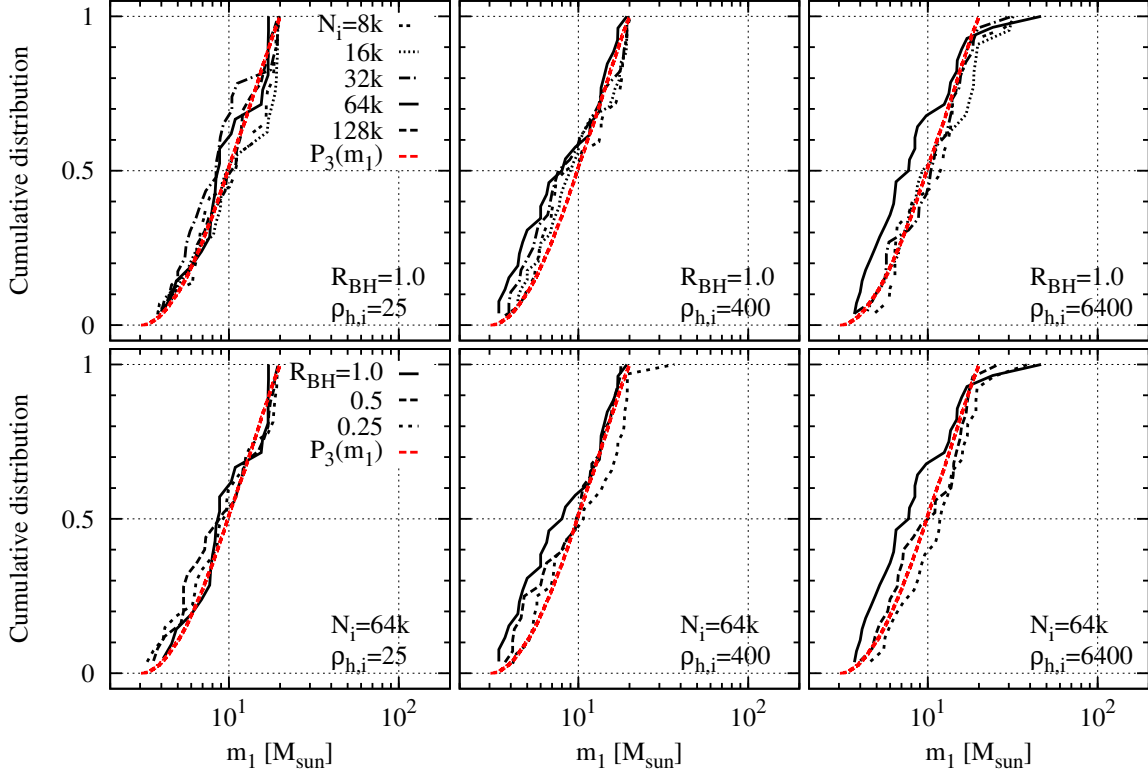**Figure 9.** Cumulative distribution of eccentricities, e, of BBH escapers. Curves with the same line types indicate the same N_i among the top panels, and the same R_{BH} among the bottom panels. Red dashed curves indicate the thermal distribution, expressed as equation (10).

Figure 10. Cumulative distribution of primary masses, m_1, of BBH escapers. Curves with the same line types indicate the same N_i among the top panels, and the same $R_{\rm BH}$ among the bottom panels. Red dashed curves show a fitting function for these cumulative distribution. The method to draw the fitting function is described in the main text.

The volume $dV(t_u)$ is expressed as

$$dV(t_u) = 4\pi D_p^2 dD_p, \quad (18)$$

where D_p is a proper distance. The proper distance is expressed as

$$D_P = \int_{t_u}^{t_{u,0}} [1 + z(t_u)] \, dt_u. \quad (19)$$

We calculate $\Gamma_{\rm det}(t_u)$ as

$$\Gamma_{\rm det}(t_u) = \int_{C_{\rm det}>1} dm_1 dq \frac{d\Gamma_{\rm mrg}(t_u)}{dm_1 dq}. \quad (20)$$

A variable $\Gamma_{\rm mrg}(t_u)$ is a merger rate of BBH escapers at a universe age t_u, where these BBH escapers originate from one GC. A variable $C_{\rm det}$ indicates a detectability of BBH escapers, and depends on m_1, q, t_u (i.e. a distance between an observer and a source), and a GW observatory. Note that BBH escapers can be detected if $C_{\rm det} > 1$. The merger rate $\Gamma_{\rm mrg}(t_u)$ is given by

$$\Gamma_{\rm mrg}(t_u) = \int_{t'_u=t_{u,0}-t_0}^{t'_u=t_u} dN_{\rm BBH,esc}(t'_u)D(t_u - t'_u), \quad (21)$$

where t_0 is the GC age at the present time, $N_{\rm BBH,esc}(t_u)$ is the total number of BBH escapers from one GC at the universe age t_u, and $D(t_u - t'_u)$ is the distribution of time delay between the time when BBHs escape and the time when the BBHs merge. Using equation (7), we can rewrite

equation (21) as

$$\Gamma_{\rm mrg}(t_u) = 0.020 N_{\rm BH,i}$$
$$\times \int_{t_{u,0}-t_0}^{t_u} dt'_u D(t_u - t'_u) \left. \frac{d\tau}{dt} \right|_{t=t'_u-(t_{u,0}-t_0)}, \quad (22)$$

where

$$N_{\rm BH,i} = 190 R_{\rm BH} \left(\frac{N_i}{128k} \right). \quad (23)$$

The derivative $d\tau/dt$ is obtained in section 4.3.

BBH escapers merge through GW radiation. Their merging timescales are estimated as

$$t_{\rm GW} = \frac{5}{256} \frac{c^5}{G^3} \frac{a^4}{m_1^3 q(1+q)} g(e), \quad (24)$$

where

$$g(e) = \frac{(1-e^2)^{3.5}}{1 + (73/24)e^2 + (37/96)e^4}. \quad (25)$$

The constant c is the light speed. Distribution function of BBH escaper properties, $p(a,e,m_1,q)$, is approximated as follows. Primary masses of BBH escapers, m_1, depends on a thermodynamical time τ as equation (14) (see also Fig. 12), which can be transformed to a physical time t. On the other hand, a, e, and q are independent of t. Therefore, we use a distribution function of BBH escaper properties, $p(a,e,q)$ at a given universe time t_u. Furthermore, a, e, and q are uncorrelated with each other. The distribution function $p(a,e,q)$
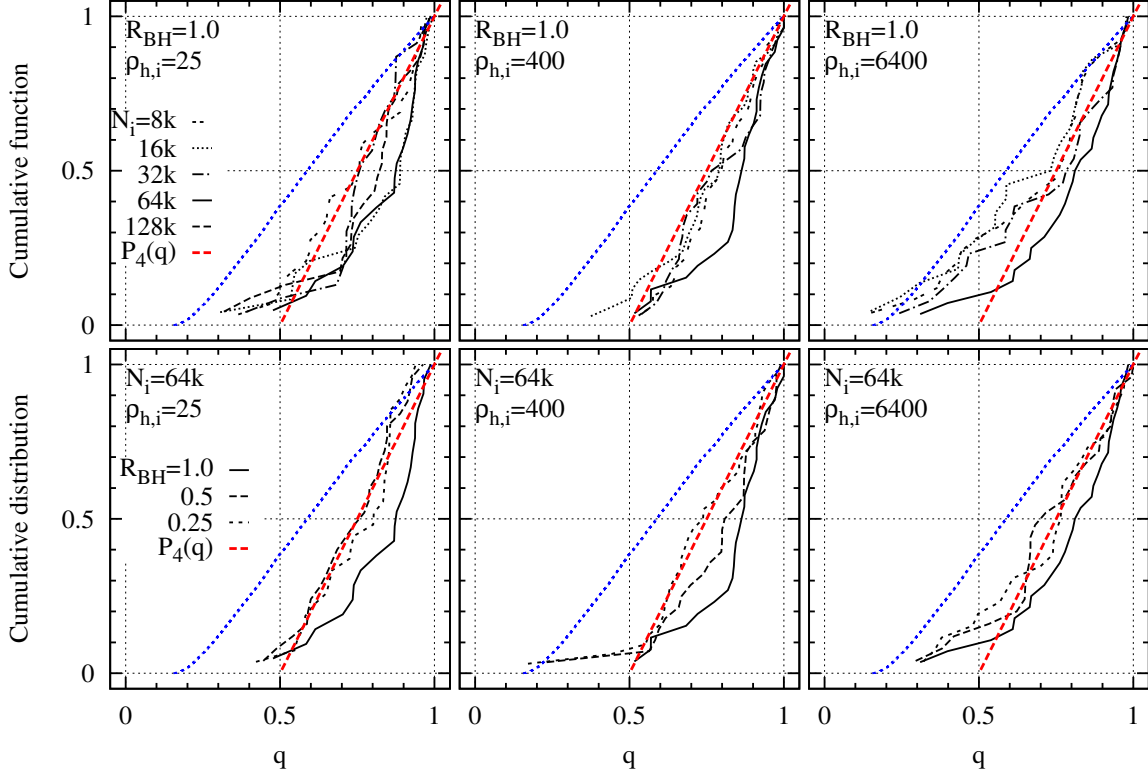
Figure 11. Cumulative distribution of the mass ratios, $q = m_2/m_1$, of BBH escapers, where m_2 is the secondary masses of BBH escapers. Curves with the same line types indicate the same N_i among the top panels, and the same R_{BH} among the bottom panels. Red dashed and blue dotted curves are drawn as described in the main text.

can be simplified as

$$p(a, e, q) = p_1(a)p_2(e)p_4(q). \tag{26}$$

The detectability of BBH escapers, C_{det}, is given by

$$C_{det} = \left(\frac{D_L}{D_{L,0}}\right)^{-1} \left(\frac{\mathcal{M}_{ch}}{\mathcal{M}_{ch,0}}\right)^{5/6} \sqrt{\frac{s(f_{off})}{s(f_{off,0})}}, \tag{27}$$

where $D_L (= [1 + z(t_u)]D_P)$ is a luminosity distance, $\mathcal{M}_{ch}$ is a redshifted chirp mass, and $s(f_{off})$ is a detector response function. The redshifted chirp mass is expressed as

$$\mathcal{M}_{ch} = [1 + z(t_u)] m_{ch}, \tag{28}$$

where m_{ch} is a chirp mass, given by

$$m_{ch} = \frac{q^{3/5}}{(1 + q)^{1/5}} m_1. \tag{29}$$

The detector response function is approximated as

$$s(f_{off}) = \int_0^{f_{off}} \frac{(f')^{-7/3}}{S_N(f')} df', \tag{30}$$

where

$$S_N(f) \propto \begin{cases} \infty & (f < 10\text{Hz}) \\ \left(\frac{f}{f_0}\right)^{-4} + 2\left[1 + \left(\frac{f}{f_0}\right)^2\right] & (f \geqslant 10\text{Hz}) \end{cases}, \tag{31}$$

with $f_0 = 70$ Hz. The cut-off frequency, f_{off}, is approximated as

$$\left(\frac{f_{off}}{\text{Hz}}\right) \sim 200 \left[\frac{m_1(1 + q)}{20M_\odot}\right]^{-1} \left[\frac{1}{1 + z(t_u)}\right]. \tag{32}$$

In order to determine $D_{L,0}$, $\mathcal{M}_{ch,0}$, and $s(f_{off,0})$, we adopt that initial LIGO and next-generation GW observatories can detect a merger of two NSs at distances of 18.4 Mpc and 300 Mpc, respectively.

4.2 Analysis models of GCs

In order to solve equation (22), we need to set up analysis models with various of N_i, $\rho_{h,i}$, and t_0. A GC age t_0 is explicitly included in equation (22). The number of BHs at the initial time, $N_{BH,i}$, depends on N_i, as seen in equation (23). The time delay distribution $D(t_u - t'_u)$ depends on semi-major axes of BBH escapers, a, via merging timescales through GW radiation (see equation (24)). As seen in section 3.3, semi-major axis distribution of BBH escapers is independent of N_i and $\rho_{h,i}$ in the unit of a_{1kT_i}, which depends on N_i and $\rho_{h,i}$ (see equation (5)). Therefore, $D(t_u - t'_u)$ is dependent on N_i and $\rho_{h,i}$.

Our choice for N_i, $\rho_{h,i}$, and t_0 is summarised in Table 2. These t_0 are in good agreement with galactic GCs. These N_i and $\rho_{h,i}$ are consistent with initial conditions of M 4 (Heggie & Giersz 2008), NGC 6397 (Giersz & Heggie 2009), and 47 Tuc (Giersz & Heggie 2011). Hereafter, we collectively refer to these models as "analysis models".

In these analysis models, NB-BBH escapers will dominate BBH escapers. The large-N_i model has the smallest half-mass relaxation time among these models. The half-mass relaxation time of the large-N_i model is almost the same as that of simulation models with $N_i = 64k$ and
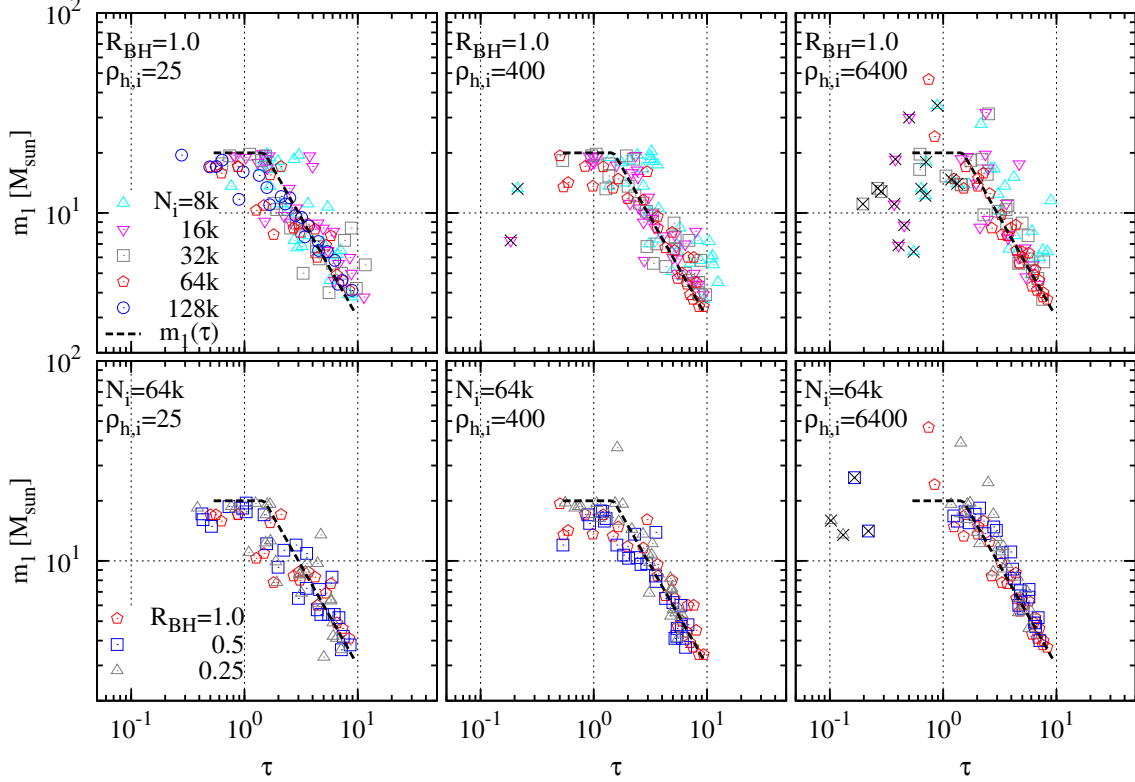
Figure 12. Primary masses of BBHs which escape from a cluster at thermodynamical time, τ. Points with the same point types indicate the same N_i among the top panels, and the same R_{BH} among the bottom panels. BBHs marked by black crosses are CE-BBHs.

Table 2. Analysis models for estimates of GW detection rates.

model	N_i	$\rho_{h,i}/M_\odot \mathrm{pc}^{-3}$	t_0/Gyr
standard	1×10^6	1.0×10^5	10
	1×10^6	1.0×10^5	12
small-N_i	5×10^5	1.0×10^5	10
	5×10^5	1.0×10^5	12
large-N_i	2×10^6	1.0×10^5	10
	2×10^6	1.0×10^5	12
small-$\rho_{h,i}$	1×10^6	6.4×10^3	10
	1×10^6	6.4×10^3	12
large-$\rho_{h,i}$	1×10^6	1.0×10^6	10
	1×10^6	1.0×10^6	12

$\rho_{h,i} = 6400$, in which the fraction of CE-BBH escapers is 10 per cent of the total BBH escapers (see the tenth column of Table 1). Since the number of CE-BBH escapers depends on half-mass relaxation time, the fraction of CE-BBH escapers will be only 10 per cent. CE-BBH escapers in the other analysis models should be smaller than those in the large-$\rho_{h,i}$ model.

4.3 Solution method

We construct fitting formula for τ as a function of t to obtain $d\tau/dt$ in equation (22) as follows. Fig. 13 shows t at τ in models with various N_i and $\rho_{h,i}$. We fit formula $N_i^x \rho_{h,i}^{-y}$ for t at each τ, where the powers x and y are indicated in Fig. 13. For this fitting, we ignore $\rho_{h,i} = 25$ models for t in the cases

of $\tau \geqslant 4$, which is justified as follows. In models with $\rho_{h,i} = 25$, τ increases, compared with t. This is because the number of stars, N, is decreased by evaporation due to strong tidal fields. On the other hand, clusters in models with $\rho_{h,i} = 400$ and 6400 are not evaporated so much, which is the case for the analysis models in Table 2. In order to obtain the relation between t and τ, we can ignore the relation between t and τ in models with $\rho_{h,i} = 25$.

Note that we may overestimate t at a given τ in the analysis models, especially at large τ. As indicated in Fig. 13, the power of $\rho_{h,i}$, y, decreases with τ increasing. This reflects the difference of evaporation between models with $\rho_{h,i} = 400$ and 6400. Clusters in simulation models with $\rho_{h,i} = 6400$ model are evaporated less than those with $\rho_{h,i} = 400$. The former clusters keep their half-mass relaxation time larger, compared with the latter clusters. If $\rho_{h,i}$ is sufficiently large, clusters are not evaporated regardless of their $\rho_{h,i}$. The power of $\rho_{h,i}$, y, should be 0.5, since half-mass relaxation time is proportional to $\rho_{h,i}^{-0.5}$ (see equation (3)). We may overestimate t in analysis models with $\rho_{h,i} = 10^5$ and 10^6. We discuss this in section 5.1.

From the formula $N_i^x \rho_{h,i}^{-y}$, we obtain t of the analysis models. Fig. 14 shows τ as a function of t in all the analysis models. For each model, we adopt fitting formulae, using third polynomial interpolations. These fitting formulae are summarised in Table 3.

In order to calculate equation (15) and (22), we discretise the integrals in these equations. We set time bins to 1 Gyr. These time bins seem too large, however are sufficiently accurate for this estimate. This is because we have
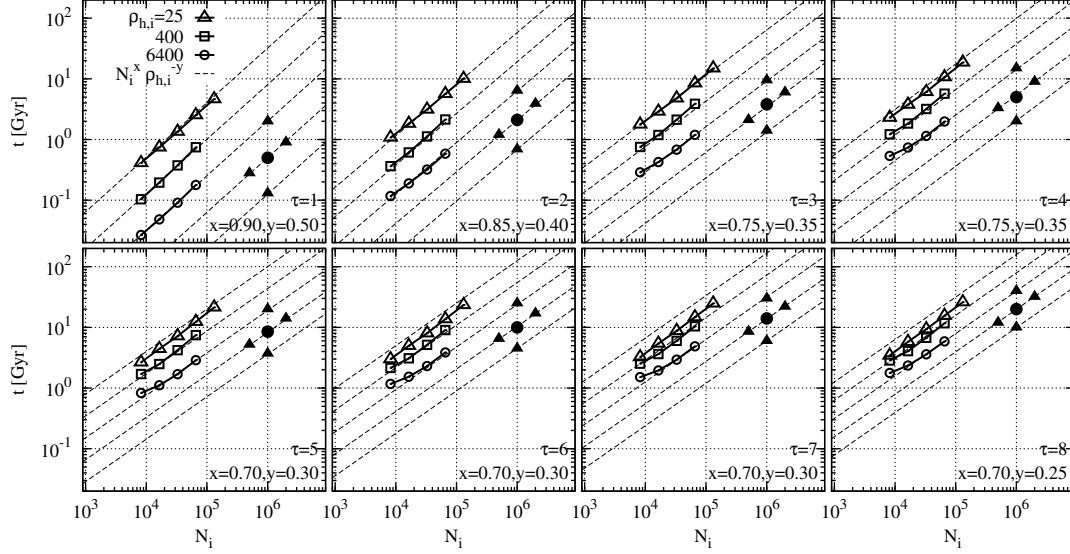
Figure 13. GC ages at thermodynamical time $\tau = 1, 2, 3, 4, 5, 6, 7$, and 8 in our cluster models. Dashed lines fit to our simulation results, indicated by open points with solid curves. Fitting formula for these dashed lines are $N_i^x \rho_{h,i}^{-y}$, where the powers x and y is written in the panels. Filled points indicate physical time in the standard (circles) and the other models (triangles), which are obtained from the fitting formula.
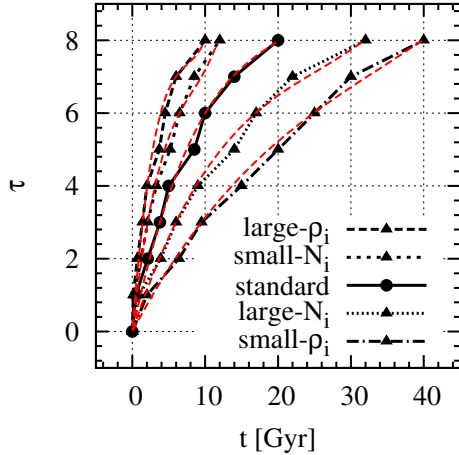

Figure 14. Thermodynamical time τ at each physical time t in the standard (filled circles) and the other models (filled triangles). Dashed red curves are obtained from third polynomial interpolation, and the fitting formulae is shown in Table 3.

Table 3. Fitting formula for $\tau = at^3 + bt^2 + ct$

model	a	b	c
standard	6.52×10^{-4}	-3.96×10^{-2}	9.30×10^{-1}
small-N_i	6.98×10^{-3}	-1.74×10^{-1}	$1.76 \times 10^{+0}$
large-N_i	2.50×10^{-4}	-1.91×10^{-2}	6.06×10^{-1}
small-ρ_i	7.29×10^{-5}	-7.40×10^{-3}	3.80×10^{-1}
large-ρ_i	1.40×10^{-2}	-3.16×10^{-1}	$2.56 \times 10^{+0}$

tain m_1. The generated BBH escapers are reutilised when equation (20) is calculated.

4.4 Detection Rate and properties of BBH escapers

Fig. 15 shows detection rates by means of next-generation GW observatories (top) and Initial LIGO (bottom) in the standard model. The detection rate is much less than 10^{-2} yr^{-1} by means of Initial LIGO, while it is more than 1 yr^{-1} by means of next-generation GW observatories. The detection rates in younger analysis models ($t_0 = 10$ Gyr) are larger than those in older analysis models ($t_0 = 12$ Gyr) by a factor of about two (see the top panel of Fig. 15). More massive BBHs escape, and merge at an earlier time, i.e. at a more distant place. Therefore, the detection rate is larger in younger analysis models.

Fig. 16 shows redshifted chirp mass distributions in the standard models. In each case of t_0 and R_{BH}, its chirp mass distribution has a sharp peak at about $5M_\odot$. This is because our simulation models have a BH mass function with a peak around at $5M_\odot$ (see Fig. 2), and because less massive BBHs merge at a later time, i.e. at a closer place. Comparing the chirp mass distributions between younger and older analysis models, we can see that a chirp mass distribution has a
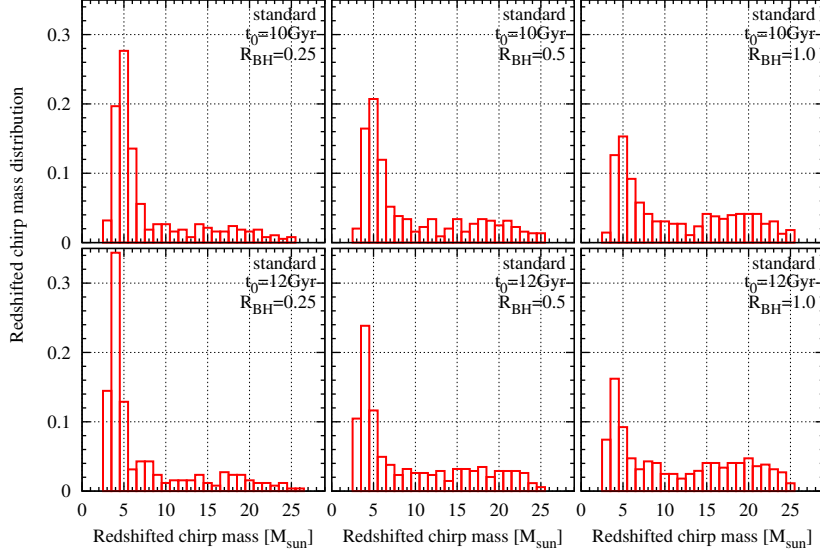
already extrapolated the number of BBH escapers, and used rough fitting formulae for a, e, m_1, and q of BBH escapers.

When we calculate the time delay distribution $D(t_u - t'_u)$ at each time bin in equation (22), we generate 10000 BBH escapers artificially as follows. We determine a, e, and q of a BBH escaper by means of Monte Carlo technique. The probability distribution of a, e, and q is obeyed by equation (26). Furthermore, m_1 is set by the universe age t_u. Here, the universe age t_u is determined as follows. We can derive τ_{min} and τ_{max} from the time bin. We obtain τ in a normal distribution between τ_{min} and τ_{max} by means of Monte Carlo technique. Finally, we convert τ to t_u, and ob-

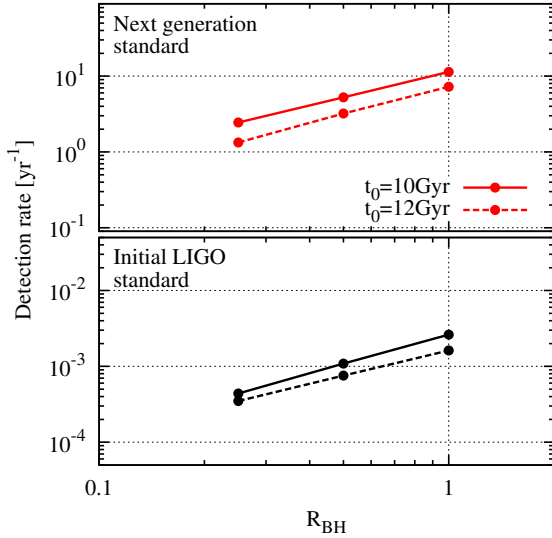**Figure 16.** Redshifted chirp mass distribution of detected BBHs in the standard model.

Figure 15. Detection rates as a function of BH retention fraction R_{BH} in the standard model by means of next-generation GW observatories (top) and Initial LIGO (bottom). In each panel, the detection rates are indicated by solid and dashed curves, when the ages of GCs, t_0, are 10 Gyr and 12 Gyr, respectively.

Figure 17. Detection rates (black points with curves) as a function of BH retention fraction R_{BH} in models other than the standard model by means of next-generation GW observatories. For comparison, the detection rates in the standard model are indicated by red points with curves. In each panel, the detection rates are indicated by solid and dashed curves, when the ages of GCs, t_0, are 10 Gyr and 12 Gyr, respectively.

peak at more massive chirp mass in younger analysis models in each R_{BH} model; younger and older GCs have a peak at $5M_\odot$ and $4M_\odot$, respectively. This is consistent with the above argument that more massive BBHs merge in younger analysis models at a given universe time (or at a given place). The peaks in younger and older analysis models becomes sharper as R_{BH} decreases. More massive BBHs merge at an earlier time in smaller R_{BH} models, and are harder to be detected. This is because BBH escapers have smaller semi-major axes in smaller R_{BH} models (see Fig. 7), i.e. smaller merging timescales.
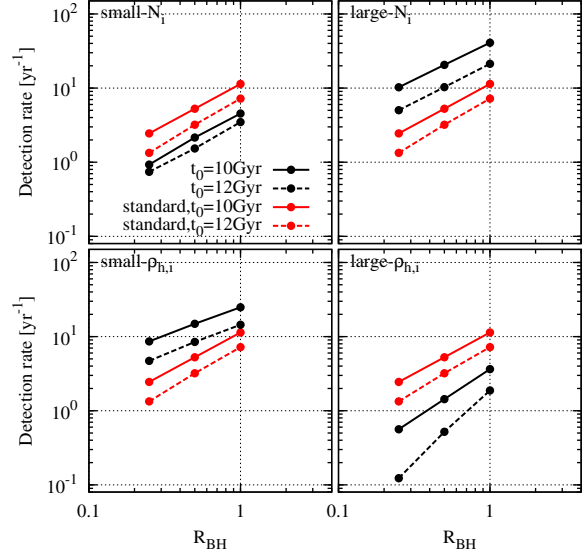
Fig. 17 shows detection rates in models other than the standard models (black points with curves). The detection rates in the small-$\rho_{h,i}$ and large-N_i models are larger than those in the standard models, while those in the large-$\rho_{h,i}$ and small-N_i models are smaller. Half-mass relaxation time in the former models is larger than that in the standard models. Therefore, the clusters evolve more slowly, and more massive BBHs escape, and merge at a later time (or at a closer place). Eventually, the detection rates become larger
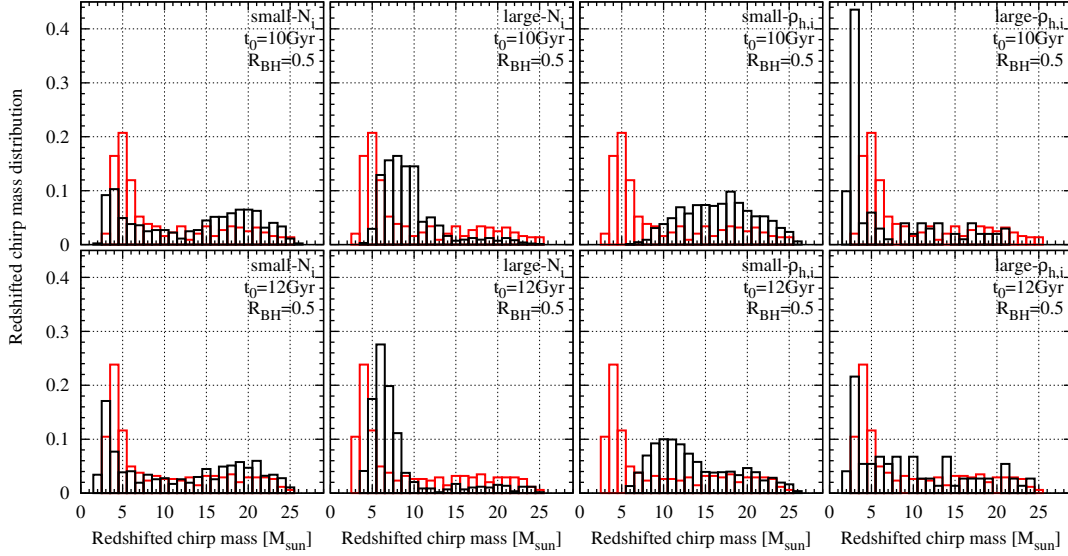
Figure 18. Redshifted chirp mass distribution of detected BBHs in the standard (red) and the other models (black), where BH retention fraction $R_{\rm BH} = 0.5$, and the age of GCs $t_0 = 10$ Gyr (top panels) and $t_0 = 12$ Gyr (bottom panels).

than the standard models. In the latter models, the opposite happens.

Fig. 18 shows redshifted chirp mass distribution of merged BBH escapers in models other than the standard model. Chirp mass distributions in the large-$N_{\rm i}$ and small-$\rho_{\rm h,i}$ models have peaks at larger masses than those in the standard models. In these models, clusters evolve more slowly than in the standard models. More massive BBHs escape, and merge at a later time. Conversely, in the large-$\rho_{\rm h,i}$ models, the peak has $3M_\odot$, which is smaller than in the standard models. In this model, clusters evolve more rapidly, and more massive BBHs escape and merge at an earlier time. In the small-$N_{\rm i}$ model, we can see two peaks at $4M_\odot$ and $20M_\odot$ in $t_0 = 10$ Gyr case. The smaller peak, which is smaller than that at the peak in the standard model, can be explained by the reason similar to the above. In the small-$N_{\rm i}$ model, clusters evolve more rapidly than in the standard model, and more massive BBHs escape, and merge at an earlier time. The larger peak comes from larger semi-major axes of BBH escapers, i.e. their larger merging timescales, due to small $N_{\rm i}$. Since massive BBHs which escape at an early time have larger merging timescales, the larger number of massive BBHs before merge is left in this model than in the standard model.

We show cumulative distributions of mass ratios of detected BBHs in Fig. 19. The cumulative distributions are almost the same regardless of analysis models. The mass ratios of detected BBHs shift to unity, compared with those of the generated BBHs. This is because BBHs with larger mass ratios are more likely to be detected. Conservatively speaking, it may come from an artificial effect that the mass ratios are almost the same. When we generate BBH populations, we adopt the same probability distribution of the mass ratios, whenever BBHs escape. This is because we do not find any correlation between the mass ratios and physical time (or thermodynamical time) in our simulations. However, the number of BBH escapers in our simulations may be statistically poor in order to reveal a correlation between the mass
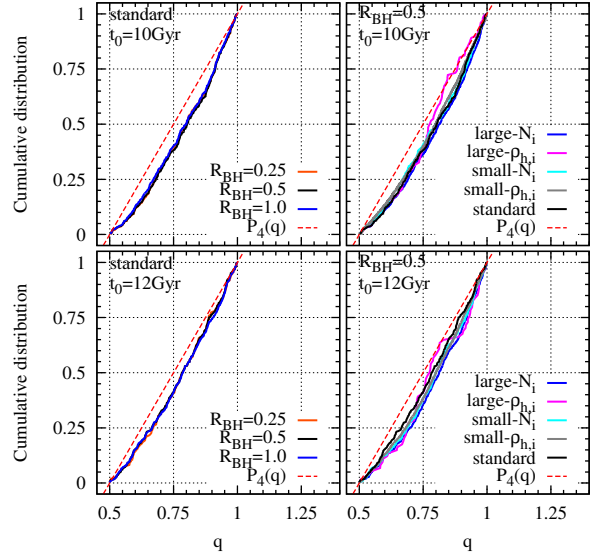

Figure 19. Cumulative distribution of mass ratios of detected BBHs. Analysis models, GC ages, and BH retention fractions are indicated in each panel. Red dashed lines in all the panels are fitting formula for cumulative distribution of the mass ratios, which are the same as red dashed lines in Fig. 11.

ratios and the time when BBHs escape. Nevertheless, we emphasise the importance that the mass ratio distribution is independent of analysis models, since this can be a clue to make clear a dominant BBH formation process.

5 DISCUSSION

5.1 Uncertainty in our estimate

In previous sections, we obtain a detection rate of BBH mergers by GW observatories by simplification in many

points. In this section, we discuss effects of these simplifications on our estimate.

First, our simulations only span one order of magnitude in N_i, 10^4 – 10^5. It is uncertain that the N_i dependence observed in our simulations continues to $N_i \sim 10^6$. This uncertainty affects many quantities, such as the number of BBH escapers, semi-major axes of BBH escapers, and the relation between t and τ. We note that the uncertainty of N-dependence is inherent in our estimate of BBH detection rates.

We also extrapolate $\rho_{h,i}$ by using $\rho_{h,i}$ dependence, and often ignore results in simulation models with $\rho_{h,i} = 25$. It is not trivial to apply results in simulation models with $\rho_{h,i} = 400$ and 6400 to estimate of BBH detection rate in analysis models with $\rho_{h,i} > 10^5$. Clusters with $\rho_{h,i} > 10^5$ are less evaporated than those with $\rho_{h,i} = 400$ and 6400. This difference can affect $\rho_{h,i}$ dependence of the number and semi-major axes of BBH escapers. Considering the difference of the number and semi-major axes between models with $\rho_{h,i} = 25$ and models with $\rho_{h,i} = 400$ and 6400, we may underestimate the number of BBH escapers, and overestimate the semi-major axes of BBH escapers. It is unclear whether we overestimate or underestimate BBH detection rate. BBH detection rate increases with the number of BBH escapers increasing, however decreases with the semi-major axes of BBH escapers decreasing, since BBH escapers merge at an earlier time, i.e. at a more distant place.

As described in section 4.3, we may overestimate a physical time of an analysis model at a given thermodynamical time, and underestimate a speed of its dynamical evolution. If this is true, BBHs are formed, and escape from clusters at an earlier time than we estimate in section 4.4. Then, BBH escapers merge at a more distant place, and are harder to be detected. Eventually, the BBH detection rates are decreased, and the peaks of chirp mass distribution shift smaller masses in all the analysis models.

We model BH natal kick, such that BHs are ejected from a cluster with a fixed probability, independently of BH masses. Since our initial stellar mass function is top-light (see equation (1)), BH populations in our clusters have a top-light mass function, as seen in Fig. 2. However, a BH mass function in reality may not be top-light. Belczynski et al. (2006) have published BH mass functions in young stellar clusters. Their fig. 6 shows that BH mass function has two peaks at $10 - 16 M_\odot$, and at $22 - 26 M_\odot$. There are few BHs with less than $10 M_\odot$ in contrast with our BH mass function. The difference between our and their BH mass functions comes from models of BH natal kick. They have adopted a model of BH natal kick velocity inversely proportional to BH masses. Our BH mass function may contain more BHs with $< 10 M_\odot$ than in reality.

In our simulation models, we adopt metallicity $Z = 0.001$, which is one of two peaks in a metallicity distribution of GCs. The other peak is at $Z = 0.02$. As metallicity becomes larger, stellar wind becomes strong, and BH mass becomes smaller. Nevertheless, our BH masses are smaller than BH masses at $Z = 0.02$ (Belczynski et al. 2006).

We do not consider primordial binaries. The primordial binaries should contain binaries consisting of two BH progenitors. Some of these binaries should be compact enough to survive against external perturbations from other cluster stars. They can experience common envelope evolution, and become CE-BBHs, or single BHs because of BH progenitor mergers. Eventually, our models may underestimate the relative importance of CE-BBHs and single BHs whose progenitors experience mergers. However, we mention that CE-BBHs are formed in our simulations more easily than in reality. We include no natal kick in a part of BHs. If these BHs form CE-BBHs, the CE-BBHs are not disrupted. In reality, BHs should receive natal kick velocities less than escape velocities of clusters. This natal kick may disrupt CE-BBHs.

We also ignore primordial mass segregation. If we consider primordial mass segregation, massive stars are initially concentrated at the cluster centre. This effect should increase the number of massive stars which experience common envelop evolution, and which merge with another massive star.

BBH escapers in our simulation results slightly contain BBHs in hierarchical triple systems. We have found such BBHs in a part of cluster models; for example, one BBH of 28 BBHs is included in hierarchical triple systems in a cluster model with $N_i = 64k$, $\rho_{h,i} = 6400$, and $R_{BH} = 1.0$. However, such BBHs can be increased if primordial binaries are considered. This is because binary-binary interactions leave hierarchical triple systems at a significant rate (Mikkola 1983, 1984). BBHs in hierarchical triple systems are secularly perturbed by the third stars, and change their eccentricities periodically (Kozai 1962). BBHs in hierarchical triple systems have smaller merging timescales than those in isolation (Miller & Hamilton 2002; Blaes, Lee & Socrates 2002; Thompson 2011; Pejcha et al. 2013; Seto 2013). Therefore, we may overestimate the merging timescales of BBH escapers.

In summary, our BH mass function may have too top-light shape as compared to a BH mass function in reality. It is unclear that these increase or decrease the BBH detection rate. More massive BBHs escape, and merge at an earlier time. However, they are detected more easily owing to larger chirp masses. BBHs in hierarchical triple systems also merge at an earlier time, which may decrease our BBH detection rate.

So far, we ignore the detection of BBH mergers inside GCs. Our simulations results show that some of BHs remain in GCs with the standard, large-N_i, and small-$\rho_{h,ii}$ models. This is consistent with a recent observation of Strader et al. (2012), who have found in M22 two radio sources which seem BHs. These BHs should form BBHs. Although BBHs in GCs have larger semi-major axes than BBH escapers, they should be frequently perturbed by other stars, have very high eccentricities by chance, and merge. In this sense, we may underestimate the detection rate of BBH mergers.

5.2 Comparison with previous studies

In this section, we compare our estimate with previous ones. It is difficult to compare these estimates, since both of numerical methods and simulation models, such as BH mass functions, are different. If we ignore the difference of numerical methods, our estimate $(0.3 - 10 \text{ yr}^{-1})$ is consistent with the estimates of O06 $(1 - 10 \text{ yr}^{-1})$, and D10 $(1 - 100 \text{ yr}^{-1})$, except that of S08 $(25 - 3000 \text{ yr}^{-1})$, although BH mass functions are completely different. BBH detection rates may be weakly dependent on BH mass functions. However, we need

to confirm whether we get similar estimates to those of O06 and D10 if we adopt the same BH mass functions as theirs. This will be our future work.

5.3 Distinction of BBH formation process

In this section, we discuss the possibility of distinction of a dominant BBH formation process, such as formation from a primordial binary on galactic fields, and dynamical formation in dense stellar clusters. From the above, a detection rate of BBHs formed in GCs should be at most 100 yr^{-1}. This is similar to a detection rate of BBHs originating from galactic fields (Abadie et al. 2010, e.g.). Note that Belczynski & Dominik (2012) have reported $10^3 - 10^4$ yr^{-1}. It may be difficult for detection rates to make clear a dominant BBH formation process.

A mass ratio distribution can be promising for its distinction. As described in section 4.4, the mass ratio distribution is independent of analysis models. However, we postpone trying to use mass ratio distribution. Mass ratio distribution will strongly depend on BH mass functions. In our future work, we will investigate dependence of mass ratio distributions on BH mass functions, and search for a method of the distinction of a dominant BBH formation processes.

As a chirp mass distribution is different among analysis models, the distribution may be useful to know GC initial conditions. Chirp mass distribution will also depend on BH mass functions. In future work, we will also seek its dependence.

6 SUMMARY

We have performed N-body simulations in order to estimate the detection rate of mergers of BBHs originating from GCs by means of GW observatories. We have also obtained their distributions of chirp masses and mass ratios. N-body simulations can not deal with a GC with $N \sim 10^6$ due to the lack of computing power. Instead, we have performed N-body simulations of small-N clusters ($N_i = 8k - 128k$), and have extrapolated their results to large-N clusters.

This extrapolation can be done, using the following properties of BBH escapers. BBHs are ejected from the clusters at a rate proportional to N_i in the unit of τ. The semi-major axis distribution of BBH escapers are independent of N_i in the unit of a_{1kT_i}, i.e. inversely proportional to N_i in physical units. The distributions of eccentricities, primary masses, and mass ratios of BBH escapers are independent of N_i. We have estimated the detection rate of BBH mergers by the next-generation GW observatories. The detection rate is $0.1 - 10$ yr^{-1} for $R_{BH} = 0.25$, $0.5 - 20$ yr^{-1} for $R_{BH} = 0.5$, and $2 - 40$ yr^{-1} for $R_{BH} = 1.0$. The difference of the detection rates in each R_{BH} comes from initial conditions of GCs, such as N_i, $\rho_{h,i}$, and t_0.

Our estimate of a BBH detection rate is almost the same as previous studies of BBHs in GCs (O06; D10; D11). Furthermore, it is similar both to those of BBHs formed in galactic centres (O'Leary, Kocsis & Loeb 2009), and to those of BBHs formed on galactic fields (Abadie et al. 2010). These BBH detection rates can not distinguish a dominant BBH formation process.

A mass ratio distribution of BBHs is independent of

GC initial conditions. It may be a clue to constrain a BBH formation process. In future work, we will investigate the mass ratio distributions in various type of BBH mass functions, and compare them with those on galactic fields. Since a chirp mass distribution of BBHs is sensitive to GC initial conditions, this distribution may make clear GC initial conditions, if detected BBHs are dominantly formed in GCs.

REFERENCES

Aarseth S. J., 2003, Gravitational N-body Simulations: Tools and Algorithms. Cambridge University Press, Cambridge
Abadie J. et al., 2010, Classical and Quantum Gravity, 27, 173001
Abbott B. P. et al., 2009, Reports on Progress in Physics, 72, 076901
Accadia T. et al., 2011, Classical and Quantum Gravity, 28, 4002
Acernese F. et al., 2008, Classical and Quantum Gravity, 25, 184001
Banerjee S., Baumgardt H., Kroupa P., 2010, MNRAS, 402, 371
Belczynski K., Sadowski A., Rasio F. A., Bulik T., 2006, ApJ, 650, 303
Belczynski K., Taam R. E., Kalogera V., Rasio F. A., Bulik T., 2007, ApJ, 662, 504
Belczynski K., Dominik M., 2012, preprint (arXiv:1208.0358)
Blaes O., Lee M. H., Socrates A., 2002, ApJ, 578, 775
Breen P. G., Heggie D. C., 2013, MNRAS, in press
Cohn H., Hut P., Wise M., 1989, ApJ, 342, 814
Dominik M., Belczynski K., Fryer,C., Holz D. E., Berti E., Bulik T., Mandel I., O'Shaughnessy R., 2012, ApJ, 759, 52
Downing J. M. B., Benacquista M. J., Giersz M., Spurzem R., 2010, MNRAS, 407, 1946 (D10)
Downing J. M. B., Benacquista M. J., Giersz M., Spurzem R., 2011, MNRAS, 416, 133 (D11)
Eldridge J. J., Tout C. A., 2004, MNRAS, 353, 87
Finn L. S., Chernoff D. F., 1993, Physical Review D, 47, 2198
Giersz M., 1998, MNRAS, 298, 1239
Giersz,M., Heggie D. C., 2009, MNRAS, 395, 1173
Giersz,M., Heggie D. C., 2011, MNRAS, 410, 2698
Harris W. E., Whitmore B. C., Karakla D., Okoń W., Baum, W. A., Hane, D. A., 2006, ApJ, 636, 90
Harry G. M. et al., 2010, Classical and Quantum Gravity, 27, 084006
Heggie D. C., 1975, MNRAS, 173, 729
Heggie D. C., Giersz M., 2008, MNRAS, 389, 1858

Hénon M., 1971, Ap&SS, 13, 284

Hinshaw G. et al., 2012, preprint (arXiv:1212.5226)

Hurley J. R., Pols O. R., Tout C. A., 2000, MNRAS, 315, 543

Hurley J. R., Tout C. A., Aarseth S. J., Pols O. R., 2001, MNRAS, 323, 630

King I., 1966, AJ, 71, 64

Kozai Y., 1962, AJ, 67, 591

Kroupa P., 2001, MNRAS, 322, 231

Kuroda K. et al., 2010, Classical and Quantum Gravity, 27, 4004

Kustaanheimo P., Stiefel E. L., 1965, J. Reine Angew. Math., 218, 204

Lück H. et al., 2006, Classical and Quantum Gravity, 23, 71

Mackey A. D., Wilkinson M. I., Davies M. B., Gilmore G. F., 2008, MNRAS, 386, 65

Mikkola S., 1983, MNRAS, 203, 1107

Mikkola S., 1984, MNRAS, 207, 115

Mikkola S., Aarseth S. J., 1990, Celestial Mechanics and Dynamical Astronomy, 47, 375

Mikkola S., Aarseth S. J., 1993, Celestial Mechanics and Dynamical Astronomy, 57, 439

Miller M. C., Hamilton, D. P., 2002, ApJ, 576, 894

Nitadori K., 2009, PhD Thesis, University of Tokyo

O'Leary R. M., Kocsis B., Loeb A., 2009, MNRAS, 395, 2127

O'Leary R. M., Rasio F. A., Fegeau J. M., Ivanova N., O'Shaughnessy R., 2006, ApJ, 637, 937 (O06)

Pejcha O., Antognini J. M., Shappee B. J., Thompson T. A., 2013, preprint (arXiv:1304.3152)

Pfahl E., Rappaport S., Podsiadlowski P., 2002, ApJ, 573, 283

Portegies Zwart S. F. McMillan S. L. W., 2000, ApJ, 528, L17

Portegies Zwart S. F., McMillan S. L. W., Makino J., 2007, MNRAS, 374, 95

Sadowski A., Belczynski K., Bulik T, Ivanova N., Rasio F. A., O'Shaughnessy R., 2008, ApJ, 676, 1162 (S08)

Seto N., 2013, preprint (arXiv:1304.5151)

Spitzer L. Jr., 1987, Dynamical Evolution of Globular Clusters. Princeton, NJ, Princeton University Press, p. 40

Stodółkiewicz, 1982, Acta Astron., 32, 63

Stodółkiewicz, 1984, Acta Astron., 36, 19

Strader J., Chomiuk L, Maccarone T., Miller-Jones J., Seth A., 2012, Nature, 490, 71

Takahashi K., 1996, PASJ, 48, 691

Takahashi R. et al., 2004, Classical and Quantum Gravity, 21, 403

Tanikawa A., Yoshikawa K., Okamoto T., Nitadori K., 2012, New Astronomy, 17, 82 (Tanikawa et al. 2012a)

Tanikawa A., Hut P., Makino J., 2012, New Astronomy, 17, 272

Tanikawa A., Heggie D. C., Hut P., Makino J., 2012, preprint (arXiv:1208.4131) (Tanikawa et al. 2012b)

Thompson T. A., 2011, ApJ, 741, 14